DOI: 10.1002/ ((please add manuscript number))
Article type: Full Paper

On the Molecular Origin of Charge Separation at the Donor-Acceptor Interface

Gjergji Sini,[#,] Marcel Schubert,[#,]* Chad Risko,* Steffen Roland, Olivia P. Lee, Zhihua Chen, Thomas V. Richter, Daniel Dolfen, Veaceslav Coropceanu, Sabine Ludwigs, Ullrich Scherf, Antonio Facchetti, Jean M. J. Fréchet, Dieter Neher**

Dr. Gjergji Sini
Laboratoire de Physicochimie des Polymères et des Interfaces (LPPI), Université de Cergy-Pontoise, 5 Mail Gay-Lussac, F-95031, Cergy-Pontoise Cedex, France
Email: gjergji.sini@u-cergy.fr

Dr. Gjergji Sini, Dr. Veaceslav Coropceanu
School of Chemistry and Biochemistry & Center for Organic Photonics and Electronics, Georgia Institute of Technology, Atlanta, Georgia 30332-0400, USA

Dr. Marcel Schubert
School of Physics and Astronomy, University of St Andrews, KY16 9SS, St Andrews, United Kingdom
Email: ms293@st-andrews.ac.uk

Prof. Chad Risko
Department of Chemistry & Center for Applied Energy Research, University of Kentucky, Lexington, Kentucky, 40506, USA
Email: chad.risko@uky.edu

Steffen Roland, Prof. Dieter Neher
Institute of Physics and Astronomy, University of Potsdam, 14476 Potsdam, Germany
Email: neher@uni-potsdam.de

Dr. Olivia P. Lee
Department of Chemistry, University of California, Berkeley, CA 94720-1460, USA

Dr. Zhihua Chen, Prof. Antonio Facchetti
Flexterra Corporation, 8025 LAMON AVE, Skokie, Illinois 60077, USA

Dr. Thomas V. Richter, Prof. Sabine Ludwigs
IPOC - Functional Polymers, University of Stuttgart, Pfaffenwaldring 55, 70569 Stuttgart, Germany

Dr. Daniel Dolfen, Prof. Ullrich Scherf
Macromolecular Chemistry and Institute of Polymer Technology, University of Wuppertal, Gaußstraße 20, 42119 Wuppertal

Prof. Antonio Facchetti
Department of Chemistry and the Material Research Center, Northwestern University, 2145 Sheridan Road, Evanston, IL60208, USA

Prof. Jean M. J. Frechet
College of Chemistry, University of California, Berkeley, CA 94720-1460, USA
Physical Science and Engineering Division, King Abdullah University for Science and Technology, Thuwal, 23955-6900, Saudi Arabia

[#] These authors share the first authorship.

Keywords: polymer solar cells, organic photovoltaics, photo current generation, donor-acceptor interfaces, non-fullerene acceptors, energy gradient, driving force, polarization, geometrical deformations

ABSTRACT

Fullerene-based acceptors have dominated organic solar cells for almost two decades. It is only within the last few years that alternative acceptors rival their dominance, introducing much more flexibility in the optoelectronic properties of these material blends. However, a fundamental physical understanding of the processes that drive charge separation at organic heterojunctions is still missing but urgently needed to direct further material improvements. Here we use a combined experimental and theoretical approach to understand the intimate mechanisms by which molecular structure contributes to exciton dissociation, charge separation, and charge recombination at the donor-acceptor (D-A) interface. We use model systems comprised of polythiophene-based donor and rylene diimide-based acceptor polymers and perform a detailed density functional theory (DFT) investigation. The results point to the roles that geometric deformations and direct-contact intermolecular polarization play in establishing a driving force (energy gradient) for the optoelectronic processes taking place at the interface. A substantial impact for this driving force is found to stem from polymer deformations at the interface, a finding that can clearly lead to new design approaches in the development of the next generation of conjugated polymers and small molecules.

1. Introduction

Single-junction organic photovoltaic (OPV) devices are generally comprised of bulk heterojunction (BHJ) active layers derived from polymer (donor, D)–fullerene (acceptor, A) blends, which now have power conversion efficiencies (PCE) reaching 11.7%.[1] However, fullerene-based acceptors present several drawbacks, such as weak light absorption efficiency, limited potential for tuning the electronic levels, and high synthetic costs. Recent progress in the design of non-fullerene small molecule and polymeric acceptors has resulted in solar cell PCEs that now reach 11.3%[2-4] and 8.3%[5-6], respectively, rivaling fullerenes for the first time since the discovery of the electron transfer at organic D-A interfaces. Ultimately, fullerene-free OPV offer greater thermal stability,[4] increased lifetimes,[7] higher flexibility[8] and widely tunable[5] optoelectronic properties.

Among the reasons for the long-lasting dominance of fullerenes include (i) their general compatibility with structurally diverse donor materials, (ii) electron delocalization resulting in decreased electron-hole binding energy, and (iii) the absence of structural anisotropy allowing for isotropic intermolecular coupling and charge transport.[9-12] In contrast, even though non-fullerene organic semiconductors have been optimized with respect to their absorption energies, ionization potentials and electron affinities, and charge-carrier mobilities, it is still not possible to predict the solar cell performance of a combination of two of such organic materials. An example for this are BHJ OPVs prepared from a blend of poly(3-hexylthiophene) (P3HT) and poly([*N*,*N*′-bis(2-octyldodecyl)-naphthalene-1,4,5,8-bis(dicarboximide)-2,6-diyl]-*alt*-5,5′-(2,2′-bithiophene)) (PNDI),[13-14] which despite numerous optimization attempts, reach a PCE of only 1.3%, a value that is well below expectations given the excellent charge-carrier mobilities shown in OFET and the redox properties of these polymers.[15-16] For this blend, as for many other fullerene-free D-A blends, geminate charge recombination, an intimate process at the very first stage of charge-carrier separation, has been identified as the limiting process.[14] Interestingly, PNDI has recently set a record for all-polymer OPV demonstrating that charge separation (CS) can clearly outperform geminate charge recombination once a well-matched D-A combination has been identified.[5] Since charge generation is strongly controlled by the molecular structure, the seemingly random optimization process that is required to find the best-matching materials is the strongest evidence for a fundamental lack of understanding of the molecular origin of charge separation at the D-A interface.

Notably, the limited understanding has resulted in terminology confusion in the literature. For clarity, we recall definitions of the main physical phenomena occurring at the D-A interface during solar cell operation. First, excitons located on the donor, acceptor, or both (i) dissociate and result in the formation of interfacial D-A charge transfer (CT) states. These dissociated, but still strongly (Coulombically) bound electron-hole pairs, can subsequently either (ii) separate through electron- and hole-transfer from the interface into the respective bulk components through successive hopping steps, reported here as charge separation (CS), or (iii) can recombine. This last phenomenon will be reported hereafter as charge-transfer state recombination (CTSR) in order to avoid confusion with the more general case where carriers having already undergone a first (several) CS step(s) return back to the interface. This phenomenon that we call "reverse CS" can happen in the very early steps of CS under some intrinsic- or morphological materials conditions, and along with CTSR will be called geminate charge recombination (GCR). In the present study we mainly focus on the CTSR and CS phenomena.

With regard to the CS efficiency, important energetic driving forces are necessary to overcome the electron-hole binding energy (approximately 0.3 eV). The presence of an energy gradient near the interface and its contribution to the driving force for electron-hole separation is still a matter of debate.[17-23] In a simplistic framework, this effect corresponds to a larger donor ionization potential (often discussed in terms of the highest-occupied molecular orbital (HOMO) energy) and smaller acceptor electron affinity (often referenced to the lowest-unoccupied molecular orbital (LUMO) energy) at and near the D-A interface, as compared to the respective bulk energies. While different origins for this effect have been put forward, we focus in this study on the impact of the geometrical deformations and electrostatic effects on the energy gradient in the case of all-polymer BHJ OPVs.

The general dichotomy between the intrinsic properties of pristine organic semiconductors and the limited photovoltaic performance within a D-A combination reveals the complexity of the physical processes taking place in an OPV, and in particular at the D-A interface. In addition, the overwhelming number of new chemical structures that are continuously developed and the high structural complexity of the most recent organic semiconductors, especially the widely used donor-acceptor-type copolymers, impede a systematic examination about what kind of structural characteristics might be essential to enforce efficient charge carrier separation. Only very few experimental studies exist that have identified a general correlation between molecular structure and device efficiency.[24-25] It was found that replacing, for instance, the alkyl side chains on

polythiophene-based donor polymers with phenyl-containing side chains (POPT, see **Figure 1a**) results in a general increase of the short-circuit current for a wide variety of acceptors including polymers (polyphenylenevinylene (PPV) and PNDI) and small molecules (monomeric perylene diimide (monoPDI)) (**Figure 1c**).[25] This improvement was explained by an increase in the CT state energy when compared to P3HT-containing blends, a characteristic related to the increased steric interactions and inter-chain separation arising from the orthogonally oriented phenyl groups along the POPT backbone. A similar approach was taken when optimizing the conjugated polymers PBDTTT and PTB7 (Figure 1a), two of the best performing donor polymers in combination with the fullerene $PC_{70}BM$, where the exchange of the alkoxy side chains by alkylthiophene groups (PTB7-Th, see Figure 1a) lead to an improved photocurrent and overall efficiency.[26-27] Reviewing the literature of the past four years for PTB7 containing solar cells reveals that this trend is even more pronounced for non-fullerene acceptors (Figure 1c-e), which is best seen when PTB7 and PTB7-Th are combined with the same acceptor (data points connected by a black line in **Figure 1d,e**). Importantly, the concept of aromatic or cyclic side chains is also effective in more complex backbone structure, as in PBDTBDD (Figure 1a,c).[28-29] Note that these materials are sometimes referred to as two-dimensional due to the conjugated nature of the side-chains, with larger dihedral angles between the main conjugated backbone and side chain being shown to improve solar cell efficiency.[30] More evidence for the beneficial role of aromatic side chains arises from examining the structure of the newly designed acceptor molecule ITIC (**Figure 1b**) that has set several efficiency records over the last two years.[4 31 32] This molecule comprises overall four phenyl-side chains attached to a relatively short and stiff molecular backbone pointing to a cumulative effect of the structural appearance of these side groups on either one or both components of a D-A BHJ solar cell, a conclusion that is supported by recent literature reviews.[33-34] In a similar fashion, largely twisted di- or trimeric acceptor molecules like diPDI (Figure 1b) have demonstrated a clear correlation between the dihedral angle and solar cell performance providing strong evidence that charge separation processes are highly sensitive to molecular deformations at the donor-acceptor heterojunction.[35-39] All these examples show that the design of the D-A interface plays a key role in establishing efficient charge separation. Interestingly, this structural optimization is far more important for non-fullerene OPVs for reasons that are, despite ever higher performance benchmarks, still poorly understood.

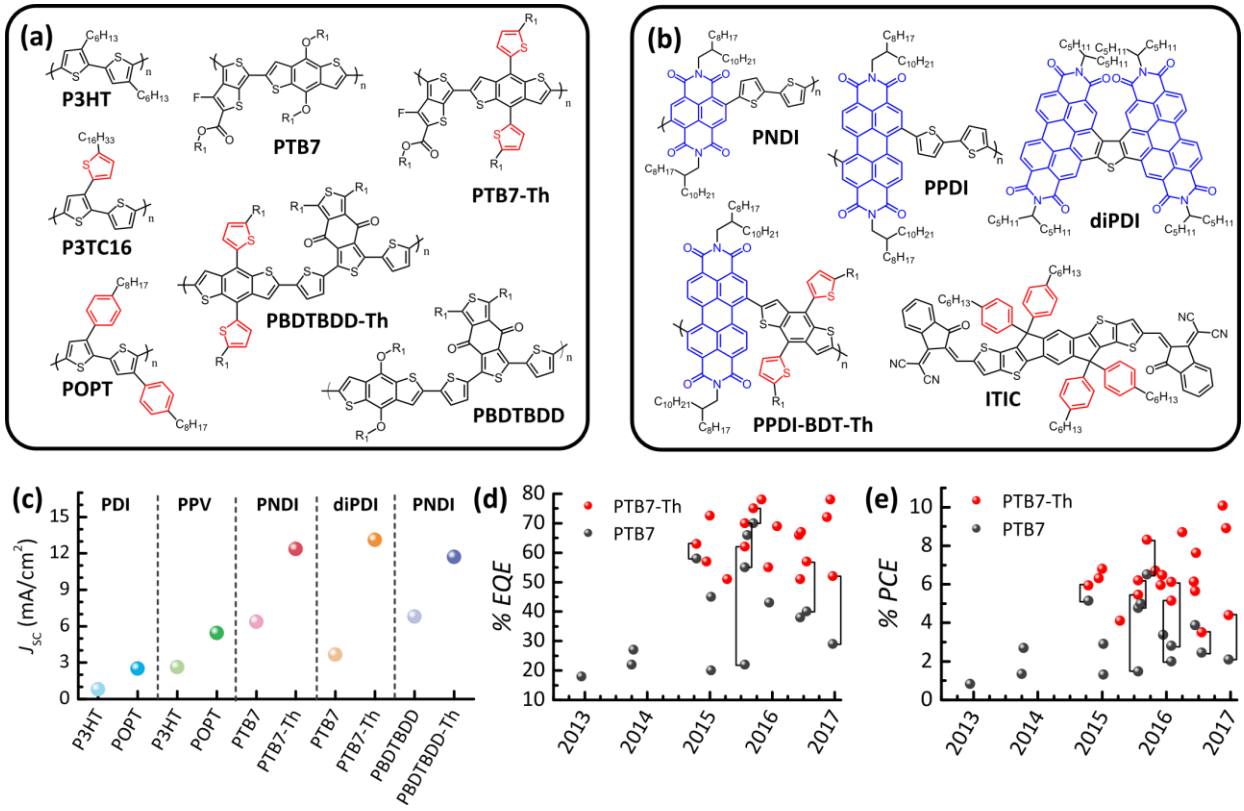

Figure 1. Influence of molecular structure on the device performance of non-fullerene organic solar cells. **(a)** Examples of donor polymer structures comprising either alkyl/alkoxy side chains or aromatic side groups (highlighted in red). R_1=ethylhexyl.**(b)** Collection of recent acceptor materials including rylene-based copolymers (containing either NDI or PDI, highlighted in blue), a dimeric PDI (diPDI) and of the high performance acceptor molecule (ITIC). **(c)** Literature examples demonstrating the beneficial role of aromatic side chains for donor polymers shown in (a). Comparison of the **(d)** PCE or **(e)** EQE of fullerene-free solar cells comprising either PTB7[35, 38, 40-50] (grey) or PTB7-Th[31, 35, 37-39, 41, 43, 46-48, 51-58] (red) as donor. Data points connected with brackets indicate that the same acceptor has been used in the study allowing for a one-to-one comparison of both donors.

Here, we aim to obtain a deeper insight into the origin of charge separation (occurring after exciton dissociation) at D-A interfaces in all-polymer BHJs, and the roles that steric interactions and redox energetics play on the CTSR and CS processes.[13-14] We first demonstrate the important role of side chains by substituting aromatic side groups on the prototypical polythiophene donor. We also explore alterations of the backbone structure in rylene-based acceptor polymers. Together, these modifications allow us to systematically increase solar cell performance. We then apply detailed computations based on the density functional theory (DFT) to deconvolute the wide range of polymer interactions helping to understand a number of the intricacies related to non-fullerene BHJ solar cells.

2. Results and Discussion

2.1. BHJ Solar Cells

To elaborate the interplay of polymer structure and charge generation, we expand our previous studies of P3HT-PNDI solar cells,[13-14] which can be seen as a prototypical D-A blend that is dominated and intrinsically limited by high geminate recombination losses.[14] Two major structural alterations were introduced with the aim to increase the efficiency of charge separation. To mimic the pronounced effect of conjugated side-chains (see Figure 1c-e), we first compare the performance of P3HT to that of donor polymers where the alkyl chains were substituted by either phenyl- (as in POPT) or thiophene-containing side chains (as in P3TC16)[59]. The second modification targets the size of the conjugated system by replacing naphthalenediimide (NDI) by perylenediimide (PDI) in two different acceptor backbone structures. The latter has been repeatedly shown to increase the photocurrent in all-polymer solar cells.[35, 60-61] Importantly, all polymers used in this study comprise a regio-regular structure which has been found to improve charge transport, molecular ordering, and charge separation.[62]

The sequence of all-polymer BHJ cells is shown in **Figure 2**, Table S1, and Figure S1, revealing that the structural alterations systematically improve the charge separation efficiency. Regarding the influence of the acceptor polymer structure by changing from PNDI to PPDI, an increase in the maximum external quantum efficiency (EQE) between 30% (POPT) and 110% (P3HT) is observed, rendering the PDI containing acceptors significantly more efficient than their NDI counterparts, consistent with previous observations. Furthermore, the effect related to the side chain substitution on the donor polymer is also apparent. By switching from P3HT to POPT, the short-circuit current (J_{SC}) and EQE both increase by 60% and 30%, for the acceptor copolymers PNDI and PPDI, respectively. This trend is even more pronounced in the internal quantum efficiency (IQE), displayed in Figure 2b, revealing that about 50% of the excitons can be split into free charges in the POPT-PPDI blend, which is 3 times larger than the maximum IQE of P3HT-PNDI. Additional solar cell systems were investigated and are shown in Figure S1, supporting the trends displayed in Figure 2. In particular, we find an improved EQE and photocurrent for the thiophene side group-containing donor polymer (P3TC16) compared to P3HT, indicating that the origin of the better charge generation is potentially related to the size rather than the exact chemical nature (i.e. thiophene or phenyl) of the side groups. Finally, we demonstrate that even in combination with a much larger CPDTDT molecular structure, the backbone substitution of NDI

by PDI significantly improves the photocurrent (Figure S1). However, the difference between the two acceptor polymers is less pronounced which we attribute to the effective dilution of the rylene units in this complex polymer structure.

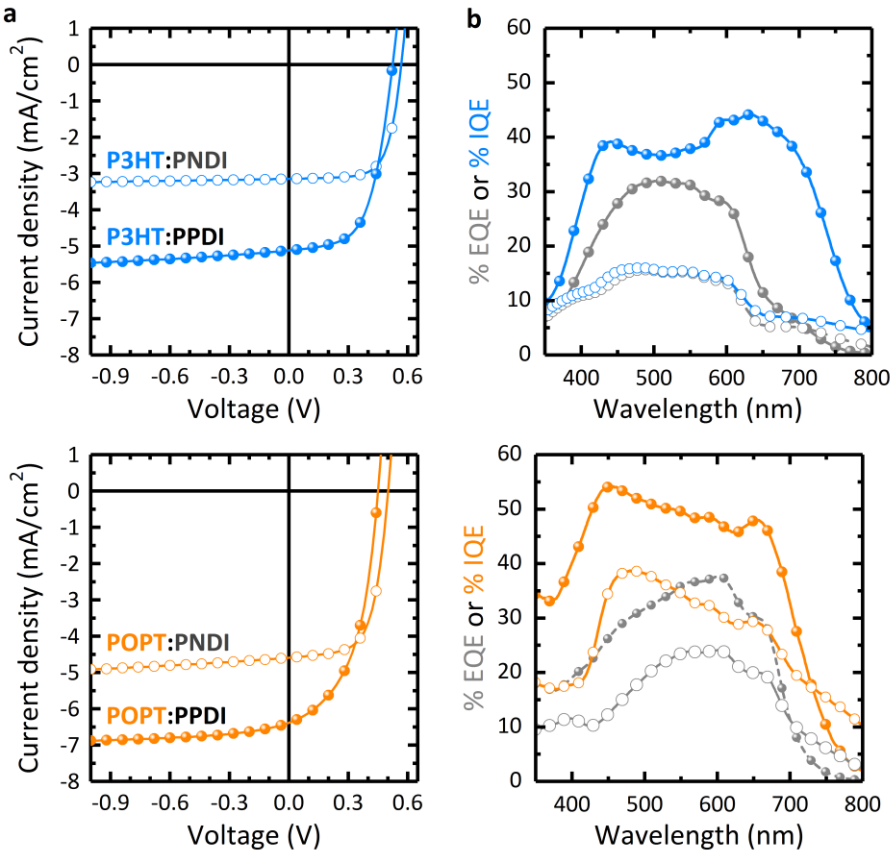

Figure 2. Solar cell characteristics of 4 blend combinations containing the donors P3HT (blue, top) and POPT (orange, bottom) and the acceptors (PNDI, open symbols) and (PPDI, closed symbols). (**a)** Current Density-Voltage characteristics under AM 1.5 G illumination, (**b)** EQE (gray) and IQE (color) for all 4 combinations.

For the solar cells displayed in Figure 2 we further characterize the photocurrent generation by performing time-delayed collection field (TDCF) experiments (Figure S2), which reveal a weak or even negligible field-dependence of the charge generation efficiency for all investigated blends, a characteristic feature of high performance solar cell systems. The direct comparison of the bias-dependent TDCF results and current-voltage characteristics in Figure S2 shows that charge recombination of free charges is very small under short circuit conditions and becomes further suppressed at reverse bias for all investigated D-A combinations. Thus, Figure 2 displays a combination of donor-acceptor pairs with systematically tunable charge generation efficiency and field-independent charge-carrier generation which mimics the structure-property relations seen in the latest high-efficiency solar cells (Figure 1c-e). Most importantly, we are able to establish this

tunable system with polymers that have a simple molecular structure, enabling us to fully analyze the underlying processes at the theoretical level.

2.2 Structural and electronic properties of the isolated oligomers

With these experimental results in hand, we now turn our attention to a density functional theory (DFT) study of the intrinsic photophysical processes at the D-A interface. A detailed description of the computational methods used here is given in the SI. Geometries of model oligomers are shown in **Figure 3**. The geometries obtained for mP3HT and mNDI ("m" standing for "model") indicate small deviations from planarity. In the case of mPDI, the steric interactions between the PDI core and the thiophene rings at the junction positions result in strong deviation of the PDI core from planarity, with dihedral angles of 25° between the four oxygen atoms. As for POPT, the phenyl groups of the isolated oligomer adopt twisted orientations with respect to the thiophenes, with dihedral angles of roughly 48° (in the central part of the 14-mer).

Select orbitals for the model donor and acceptor oligomers are shown in Figure 3. The HOMOs of the isolated mP3HT and mPOPT exhibit similar distributions along the thiophene backbone. No contributions are found on the phenyl groups of mPOPT, suggesting that these aromatic substituents impact the electronic characteristics of the solid state solely through steric interactions that dictate the interpolymer electronic coupling. As for the donor-acceptor-type model compounds mNDI and mPDI, their LUMOs contain contributions principally from two acceptor units, whereas the HOMOs are roughly localized on two bi-thiophene bridges.

HOMO and LUMO energies, ionization potentials (IPs) and electron affinities (EAs), and the theoretical $S_0 \rightarrow S_1$ excitation energies are collected in **Table 1**. Generally, the trends found from the DFT calculations follow those determined experimentally. The IP of mPOPT is larger than mP3HT by 0.24 eV, consistent with the 0.3 eV difference found experimentally.[25, 66] Similarly, the slightly larger EA for mPDI as compared to mNDI is consistent with the 0.05 eV difference found experimentally,[65] both being in line with the increased π-conjugated system and slightly lower LUMO energy in the mPDI case. Overall we obtain very good agreement between the theoretical $S_0 \rightarrow S_1$ excitation energies and the corresponding experimental values (Table 1).

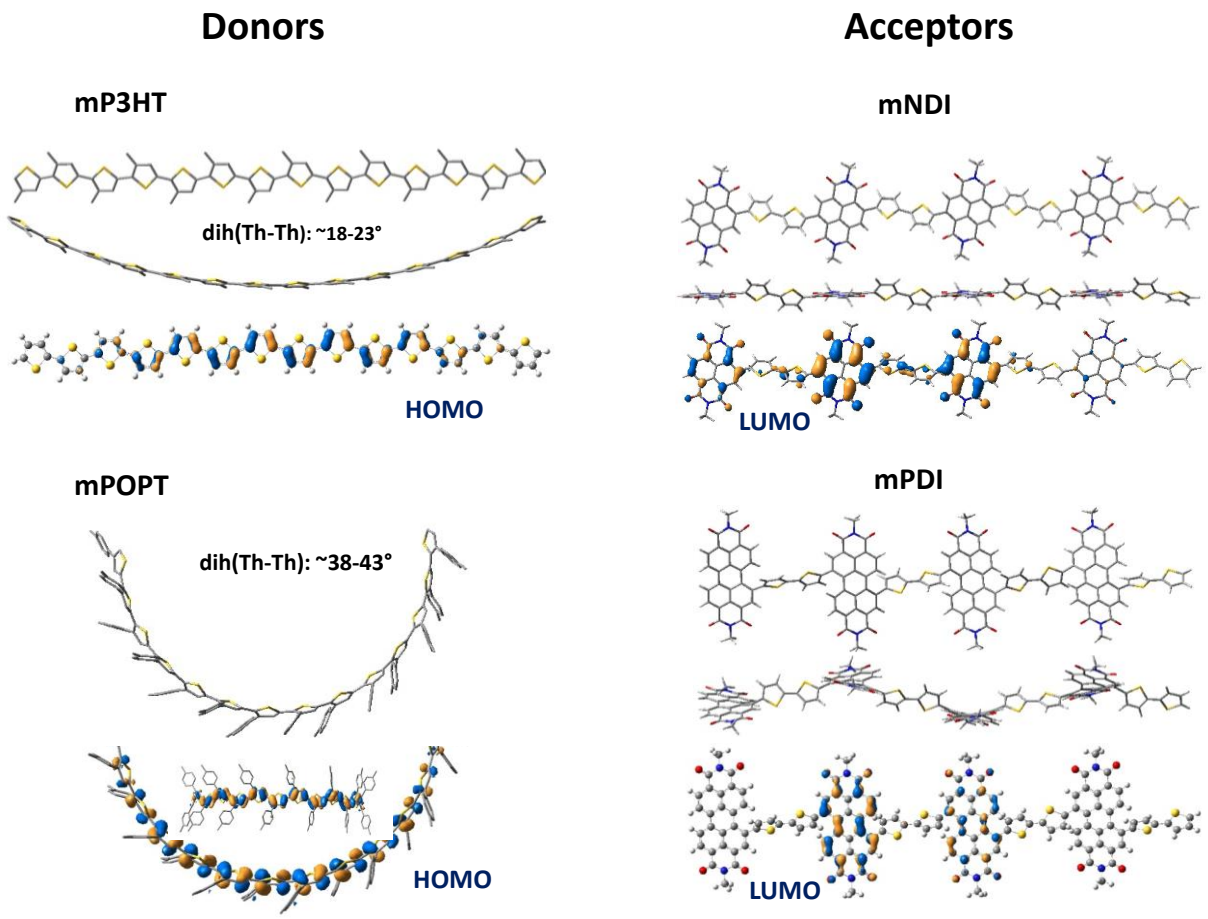

Figure 3. Shapes of isolated mP3HT, mPOPT, mNDI, and mPDI. Two views (face-on and side-on) are shown for each system, with the exception of mPOPT. The dihedral angles between the thiophene rings are indicated. The $HOMO_{donor}$ and $LUMO_{acceptor}$ of the isolated oligomer models, obtained at the B3LYP/6-31G* level of theory, are also shown (see computational methods in the SI for details on this choice). In the case of POPT, two different views of the $HOMO_{donor}$ pictogram are shown, indicating absence of contribution from the lateral phenyl groups.

Table 1. HOMO and LUMO energies, adiabatic ionization potentials (IP), electron affinities (EA), and $S_0 \rightarrow S_i$ excitation energies as calculated at the B3LYP/6-31G* level of theory for the isolated oligomer models. Experimental values are given in parentheses. All values are in eV.

	HOMO	LUMO	IP	EA	$S_0 \rightarrow S_i$
mP3HT	-4.44	-2.16	4.95 (5.2)[a]	-	2.05[b]
mPOPT	-4.77	-2.0	5.19 (5.5)[a]	-	2.09[b] (2.06, 2.52) [c]
mNDI	-5.41	-3.55	-	3.01(3.91)[d]	1.61[e] (1.45)[d]
mPDI	-5.47	-3.60	-	3.11(3.96)[d]	1.65[e] (1.65)[d]

[a] Experimental IP values taken from Holcombe et al.[25, 63] [b]Values taken in the model dimers. [c]Taken from Anderson et al.[64] [d]Taken from Chen et al.[65] [e]Correspond to $S_0 \rightarrow S_3$ transition in the dimers (f~0.3), the first transitions being of negligible oscillator strength.

2.3 Structural properties of model dimers

To understand the optoelectronic characteristics of the pure materials in the solid state, we modelled a series of oligomeric dimers. For mP3HT, mNDI, and mPDI, the average (geometry optimized) inter-molecular distance for the dimers are 3.7 Å, 3.5 Å, and 3.7 Å respectively; these values are in good agreement with solid-state interplanar distances reported for P3HT (3.8 Å)[67] and PNDI (3.9 Å).[68] In the case of mPOPT, the phenyl side chains can adopt two orientations with respect to the backbone, resulting in two structurally different dimers with interplanar distances of either 3.8 Å or 5.3 Å (see Figure S3 and Annex I in the SI for more details). The shorter intermolecular distance (3.8 Å) arises from a "flat" mPOPT backbone (Th-Th dihedral angles of 13°-19°). A more contorted mPOPT backbone (Th-Th dihedral angles of 20°-28°) stems from twisting of the phenyl groups by roughly 90° as compared to the previous conformer, giving rise to the dimer exhibiting the largest inter-molecular distance (5.3 Å). Again, very good agreement is obtained with the inter-planar distances of 3.8 Å and 5.1 Å observed experimentally.[25] Note that these structural characteristics of mPOPT dimers are strongly related with the interchain interactions between phenyl groups (Figure S3). As such, these differences are not expected to manifest in the case of POPT-acceptor interfaces.

2.4 Donor-acceptor (D-A) complexes: geometries and charge-transfer states (CTS)

We now turn to the evaluation of the geometric and electronic properties of the D-A complexes. The optimized geometries for select complexes are given in **Figure 4**. In view of the many interactions occurring among the donor and acceptor chains, the only geometrical parameter reported here (Table S2) is the average distance between the π-conjugated backbones of each fragment. Due to larger steric interactions, the average D-A distance increases when mP3HT is replaced with mPOPT and when mNDI is exchanged by mPDI. The cumulative effect of both substitutions is important, resulting in an increase of donor-acceptor average distance by 0.23 Å in the case of mPOPT-mPDI when compared to mP3HT-mNDI (3.80 Å and 3.57 Å, respectively). Importantly, strong geometric deformations are observed along the conjugated backbones of each fragment, mainly appearing as inter-ring modifications in dihedral angles. As will be shown later, these effects play a large role in the energy gradients at the D-A interface.

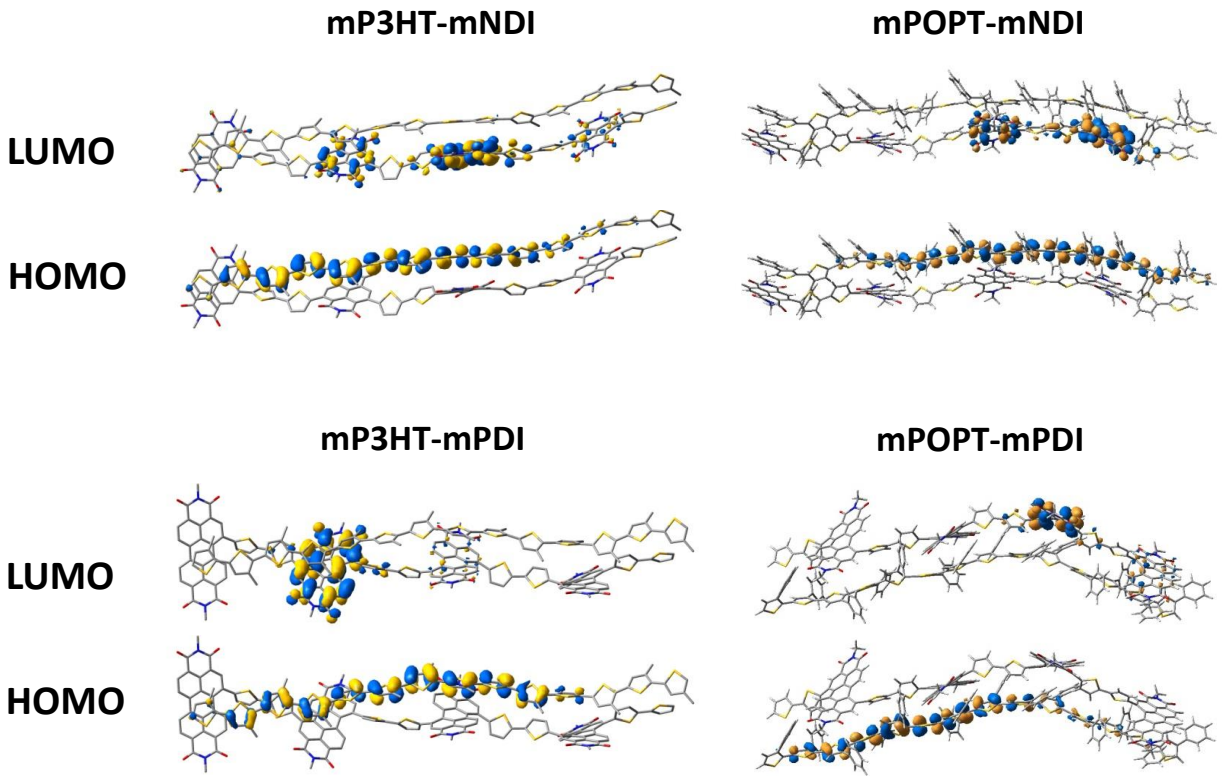

Figure 4. Global view of the optimized geometries for a selection of donor-acceptor complexes as obtained at the ωB97XD/6-31G* level in gas phase. The corresponding frontier orbitals are also shown. The choice of the ωB97XD functional is motivated by the necessity to consider long-range correction and include dispersion interactions during geometrical optimizations.

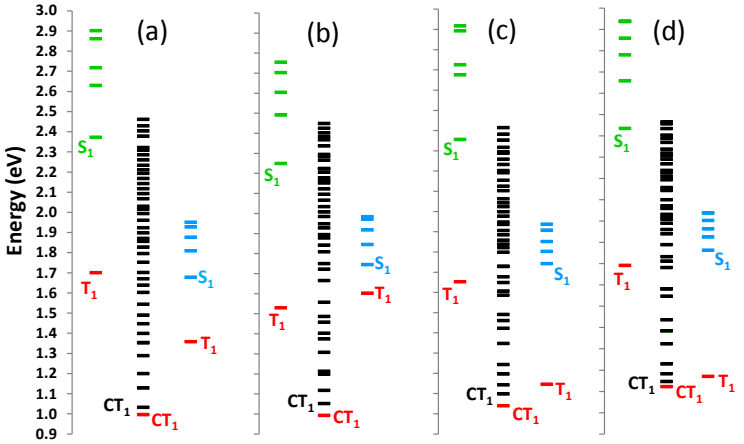

Figure 5. State-energy diagrams for (a) mP3HT-mNDI, (b) mPOPT-mNDI, (c) mP3HT-mPDI, (d) mPOPT-mPDI. Each energy level (B3LYP/6-31G*//ωB97XD/6-31G* level) corresponds to the average over three values corresponding to three isomers for each D-A complex. In each of figures a-d, the lateral level stacks correspond to five lowest local excited states for the donors and acceptors (green and blue stacks respectively, calculated at the geometry of the complex), whereas the central stacks (black) correspond to 40 excited states for each D-A complex. The red levels and labels in each diagram indicate triplet states for donors, D-A complexes, and acceptors from left to the right respectively. The isolated donor and acceptor molecules are taken at the geometry of the complex.

Figure 5 shows excited-state energy diagrams for the four D-A complexes and the isolated donor and acceptor molecules in the same geometry as in the D-A complex. The corresponding orbital energy diagrams for the isolated molecules are given in Figure S4. Initial evaluation of the four diagrams suggests that there exist a number of possible channels for exciton dissociation, which increases when NDI is substituted by PDI; this is also seen from the larger number of acceptor virtual orbitals that lie below the $LUMO_{donor}$ in mPDI when compared to mNDI (Figure S4).

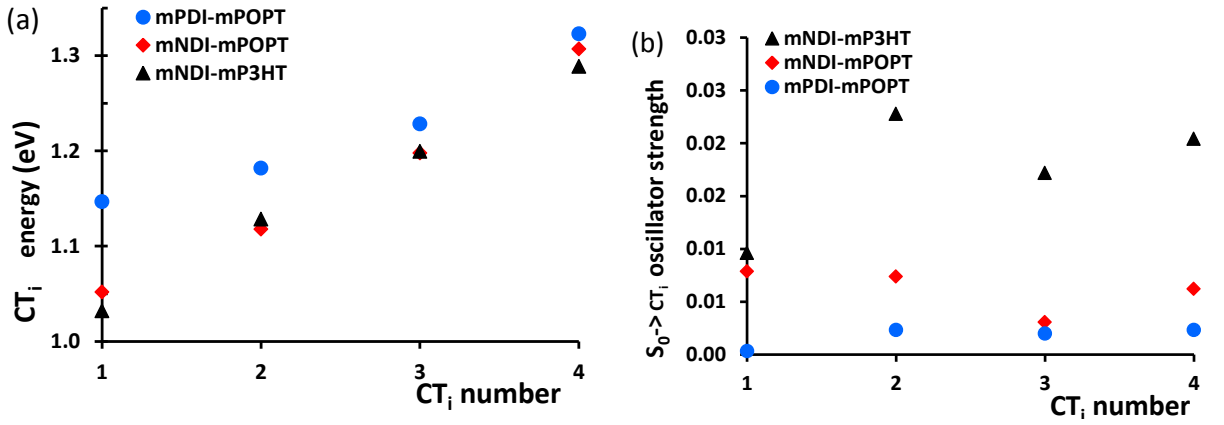

Figure 6. Electronic properties of the CT states for three different D-A complexes: (a) State-energy diagrams for the four lowest CT excited states and (b) oscillator strengths corresponding to the absorption spectra for mP3HT-mNDI, mPOPT-mNDI, and mPOPT-mPDI obtained by TDDFT calculations at the B3LYP/6-31G* level of theory.

The first four excited states for the DA complexes are pure charge transfer (CT) in character (transitions involving orbitals of pure donor- or pure acceptor nature). Their evolution across the series is shown in **Figure 6a**, indicating a global increase in the CT state energy across the series of DA complexes. We focus here on comparing the lowest CT state of each D-A complex (CT_1), given that $\Delta E(CT_1\text{-}CT_2)$ is larger than *kT* at room temperature (0.025 eV) in all cases (0.096 eV, 0.135 eV, 0.044 eV, and 0.035 eV for mP3HT-mNDI, mPOPT-mNDI, mP3HT-mPDI, and mPOPT-mPDI, respectively). The average CT_1 values vary between 1.03-1.15 eV across the D-A series (**Table 2**) in good agreement with the experimental value of 1.2 eV obtained for NDI-P3HT.[14, 69]

The $S_0 \rightarrow CT_i$ oscillator strengths, averaged over three isomers for each D-A complex, are given in Figure 6b. Globally smaller oscillator strengths are obtained when mP3HT is replaced by mPOPT, and the NDI is replaced by PDI in the acceptor oligomer. This result is consistent with the increase in the average D-A distances from 3.57 Å to 3.80 Å across the series (Table S3), thus suggesting a decrease in $S_0\text{-}CT_i$ electronic couplings with increasing oligomer separation. This effect, along

with the increase in the CT_1 energies across the series, have important consequences for the charge separation efficiency as we will discuss in the following sections.

2.5 Charge-transfer state recombination (CTSR)

Figure 7a presents a distribution of the electronic couplings in mP3HT-mNDI among several acceptor unoccupied orbitals with the $HOMO_{donor}$ – couplings that correspond to CTSR – and with the $LUMO_{donor}$ – couplings that correspond with exciton-dissociation. The averaged electronic coupling values for each D-A combination, along with other electron-transfer parameters are given in Table 2. The electronic coupling between the S_0 and CT_1 states are determined by two methods: (i) in the framework of Mulliken-Hush theory[70-72] and (ii) as a weighted sum of couplings between orbitals contributing to $S_0 \rightarrow CT_1$ excitation, based on the TDDFT B3LYP/6-31G* calculations; these results are given in Table 2 and Table S3. As a general observation, we note that the electronic couplings are larger among the acceptor-LUMO orbitals and $HOMO_{donor}$ (corresponding to CTSR) as compared to couplings with donor-LUMO (corresponding to exciton dissociation). The reason for this can be related to the better matching between the nodal planes of interacting orbitals in the case of CTSR as compared to exciton dissociation, as shown schematically in Figure S5. As a consequence, very large $S_0 \rightarrow CT_1$ couplings peaking at 0.16 eV are found (Figure 7a), whereas the electronic couplings related to exciton-dissociation remain generally smaller than 0.08 eV.[73]

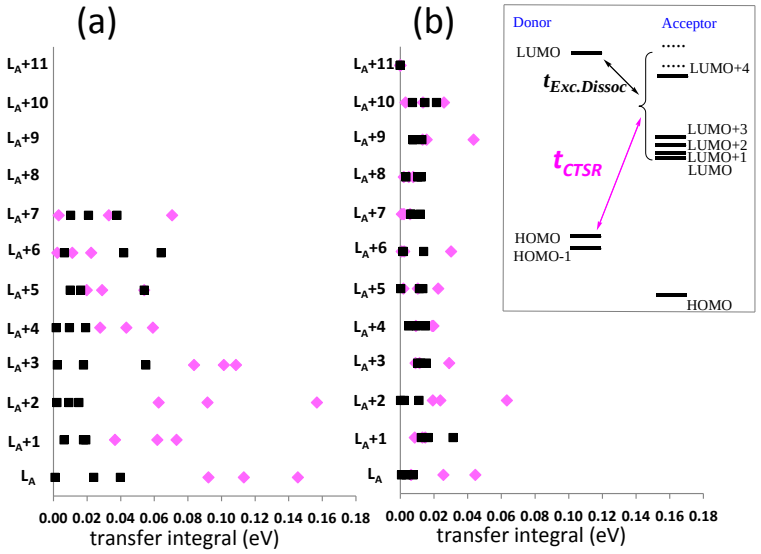

Figure 7. Electronic couplings (eV) of the $HOMO_{donor}$ with the $LUMO+n_{acceptor}$ (t_{CTSR}, pink diamonds) and of $LUMO_{donor}$ with $LUMO+n_{acceptor}$) (t_{ExDis}, black squares) associated with charge recombination and exciton dissociation, respectively for (a) mP3HT-mNDI, and (b) for mPOPT-mPDI. The interactions corresponding to t_{CTSR} and t_{ExDis} calculations are also shown schematically in the inset.

Upon substituting mP3HT with mPOPT (Figures S6b,c) and mNDI with mPDI (Figures S6d,e), the electronic couplings corresponding to CTSR decrease, with a quite important cumulative effect (Figure 7b), resulting in t_{CTSR} < 0.07 eV. A possible explanation for this effect can be given in terms of (i) increased average D-A distances from 3.57 Å to 3.80 Å, in turn resulting in decreased $HOMO_{donor}$-$LUMO_{acceptor}$ overlaps (0.011 and 0.002 for mP3HT-mNDI and mPOPT-mNDI respectively, Table 2), and (ii) the enhanced development of PDI-LUMO along the orthogonal direction as compared to the donor long axes (Figure 3), which may also contribute to the decreased $HOMO_{donor}$-$LUMO_{acceptor}$ overlap in the PDI-based complexes as compared to the NDI ones.

Table 2. Intramolecular reorganization energies corresponding to donor-acceptor charge recombination (λ_{CTSR}, eV), CTSR Gibbs free energy (taken here equal to the CT1 energy, eV), $HOMO_{donor}$-$LUMO_{acceptor}$ electronic couplings (t_{CTSR},eV) and overlaps (S_{H-L}), average distance (d,Å) between donor and acceptor backbones (standard deviations in parentheses), and rate constants (s^{-1}) for four D-A complexes calculated at the B3LYP/6-31G*//ωB97XD/6-31G* level in "gas phase". A constant value of 0.4 eV is considered for the solvent reorganization energy.

	λ_{CTSR}	E(CT_1)[a]	t_{CTSR} [a]	d [a]	S_{H-L} [a]	k_{CTSR}
mP3HT-mNDI	0.131	1.032	0.117	3.57 (0.15)	0.011	$1.1x10^{10}$
mPOPT-mNDI	0.207	1.052	0.079	3.72 (0.33)	0.006	$1.4x10^{9}$
mP3HT-mPDI	0.129	1.098	0.077	3.66 (0.33)	0.007	$5.9x10^{8}$
mPOPT-mPDI	0.205	1.147	0.025	3.80 (0.40)	0.002	$7.5x10^{6}$

[a]Average over three values corresponding to three isomers for each D-A complex.

The CTSR rates were estimated in the framework of Marcus theory (Eq. S2)[74-76] by using the electronic couplings, CT_1 energies, and intramolecular reorganization energies shown in Table 2. We also used for all systems a contribution to the reorganization energy of 0.4 eV to mimic the polarizable environment of the solid state. For mP3HT-mNDI, k_{CTSR} is calculated to $1.1x10^{10}$ s^{-1}, which is of the same order of magnitude as the geminate CR times (100-200 ps)[14] measured in the case of PNDI-P3HT. Importantly, a decrease of k_{CTSR} by three orders of magnitude upon replacing mP3HT and mNDI by mPOPT and mPDI is found, due to the cumulative effect of the decreasing electronic couplings (by roughly 5 times) and increasing driving force (CT_1 energies by roughly 100 meV). Therefore, our numerical results suggest a strong slow-down of CTSR when replacing P3HT by POPT and/or PNDI by PPDI.

2.6 Charge Separation.

We now turn to charge separation, and discuss two particular aspects: (i) the energy landscape near the D-A interface, with particular focus on the appearance and reasons for energy gradients, and (ii) the kinetics of charge separation.

Energy landscape. We focus first on the impact of two particular contributions on the frontier orbital energies at the D-A interface: (i) geometrical deformations of the polymers, and (ii) mutual electrostatic polarisation[77] between adjacent polymer chains, reported hereafter as direct-contact polarization (DCP). Additional comments on this parameter can be found in the SI.

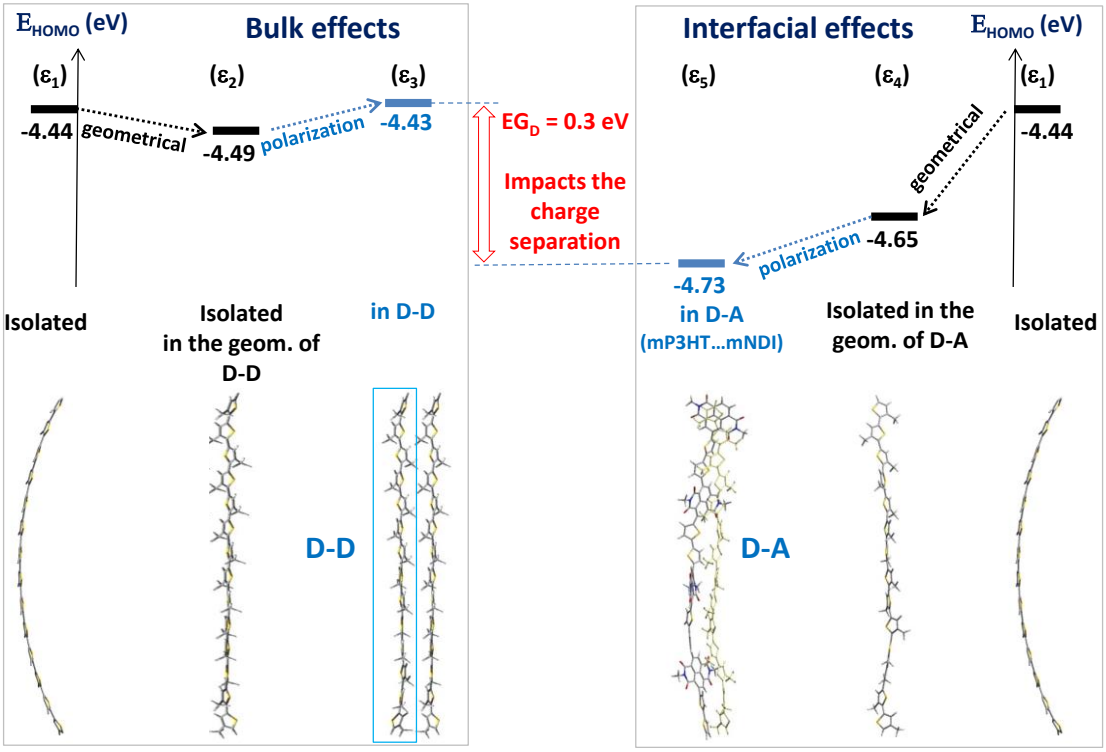

Figure 8. Energy diagram showing the evolution of the HOMO level of mP3HT in different environments (eV): (ε_1) isolated; (ε_2) isolated in the geometry of the dimer (D-D), mimicking the effect of the geometrical deformations in the bulk; (ε_3) in the geometry of the dimer (D-D) and in the presence of the second monomer, partly mimicking the additional mutual direct-contact polarization effects (DCP); (ε_4) isolated in the D-A geometry, mimicking only geometrical deformations at the interface; (ε_5) in the geometry of the donor-acceptor complex and in the presence of the acceptor, partly mimicking the DCP. The HOMO energies of mP3HT in the presence of a like molecule (dimer) or in the presence of mNDI correspond to the site energies deduced during electronic coupling calculations.

The origin of these two contributions is schematically shown in **Figure 8** by following the evolution of the mP3HT HOMO from bulk (approximated by a mP3HT dimer) to the mP3HT-mNDI interface (modelled as a D-A complex); the energy offsets related to geometric deformations and to the electrostatic polarization induced by an adjacent molecule are considered

separately and cumulatively. When compared to isolated mP3HT (ε_1 in Figure 8, -4.44 eV), the geometric deformations of mP3HT in the D-D dimer (mimicking the geometrical bulk effects) and in the D-A complexes (at the interface) result in larger HOMO energies of the mP3HT fragment due in part to reduced π-conjugation efficiency. This effect is less important in the dimers (ε_2, -4.49 eV) than at the D-A interface (ε_4, -4.65 eV). By comparing ε_2 ("geometrical-bulk") with respect to ε_4 ("geometrical- D-A interface"), an energy gradient (EG) stemming from the geometrical deformations of 0.16 eV can be deduced, constituting a driving force for charge separation; this value is quite substantial when one compares it to a typical value of 0.3 eV for the electron-hole binding energy.

The DCP effects on P3HT in the bulk as compared to the interface are found to produce opposite energy shifts (Figure 8), which can be qualitatively understood as followed: due to the mutual electron-donor effect between adjacent P3HT chains in the bulk, a higher ε_3 value as compared to ε_2 is expected, while at the D-A interface, an opposite polarisation effect occurs where due to the electron-withdrawing effect induced by the acceptor, a lower ε_5 value as compared to ε_4 value is expected. By comparing the two geometric-only values (ε_2 with respect to ε_4) and the two geometric-plus-DCP values (ε_3 with respect to ε_5), the individual contributions due to the geometrical deformations (0.16 eV) and to the DCP effects (0.14 eV) can be distinguished. The global variation between the HOMO(P3HT) at the D-A interface and in the "bulk" (0.3 eV) is shown by the red arrow (Figure 8). This energy difference reveals the establishing of an energy-gradient or energy bending at the organic-organic interfaces (reported hereafter as EG_D and EG_A for the energy gradient corresponding to the donor and acceptor respectively).

Diagrams similar to Figure 8, showing the energy gradients (EG_D and EG_A) for each D-A complex, are shown in Figure S7, with the corresponding EG numerical values collected in **Table 3** and displayed in **Figure 9**. Considering the total energy gradient (EG_{D+A}, Table 3), values ranging from 0.45-0.6 eV are determined, which are large enough to overcome the e-h binding energy. The $HOMO_{donor}$-$LUMO_{acceptor}$ energy offsets for each D-A interface ($\Delta E_{H\text{-}L}^{DA}$) deduced from Figure S7 are also given in Table 3. Overall, the $\Delta E_{H\text{-}L}^{DA}$ values increase by 0.11 eV when replacing mP3HT and mNDI with mPOPT and mPDI. It is worth noting that the $\Delta E_{H\text{-}L}^{DA}$ values are calculated by considering each compound and complex in their ground state. The global increase in CT_1 energies by the same amount (0.11 eV, Table 2) seems consequently to be due to the $HOMO_{donor}$-

$LUMO_{acceptor}$ offsets at the interface. Based on these values, the electron-hole binding energies can be calculated as $E_b^{e\text{-}h} = \Delta E_{H\text{-}L}^{DA} - E(CT_1)$. The so calculated $E_b^{e\text{-}h}$ values of 0.31 to 0.34 eV (Table 3) are consistent with the typical value of 0.3 eV, additionally indicating small $E_b^{e\text{-}h}$ variation induced by different donor-acceptor polymers.

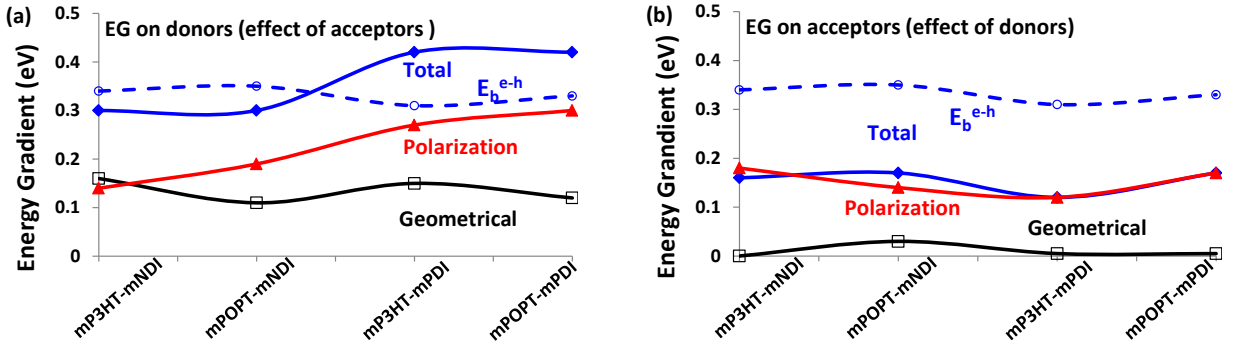

Figure 9. Energy diagrams showing the built-in energy gradient (eV, B3LYP/6-31G*) near and at the D-A interface for (a) $HOMO_{donor}$ and (b) $LUMO_{acceptor}$ corresponding to mP3HT-mNDI, mPOPT-mNDI, mP3HT-mPDI, and mPOPT-mPDI. The individual contributions (due to geometrical deformations and to direct-contact polarizations) and their sum are shown. Each value in the figure corresponds to the average out of three values. The lines have no physical meaning and are just guide for the eye. For comparison purposes, the electron-hole binding energies ($E_b^{e\text{-}h}$) are also shown by the dashed lines.

Table 3. HOMO-LUMO offsets at the D-A interface, electron-hole binding energy ($E_b^{e\text{-}h}$), energy gradient values for the donor-HOMO (EG_D), acceptor-LUMO (EG_A), and their sum (EG_{D+A}). The individual contributions of geometrical deformations and electrostatic direct-contact polarizations (DCP) are also given. Note that these EG values include both "bulk" and interfacial effects, whereas only-interfacial values are collected in Table S4. All values are in eV.

			Geometrical		Polarization (DCP)		Total		
	$\Delta E_{H\text{-}L}^{DA}$	$E_b^{e\text{-}h}$	EG_D	EG_A	EG_D	EG_A	EG_D	EG_A	EG_{D+A}
mP3HT-mNDI	1.37	0.34	0.16	-0.02	0.14	0.18	0.30	0.16	0.46
mPOPT-mNDI	1.40	0.35	0.11	0.03	0.19	0.14	0.30	0.17	0.47
mP3HT-mPDI	1.41	0.31	0.15	0.00	0.27	0.12	0.42	0.12	0.54
mPOPT-mPDI	1.48	0.33	0.12	0.00	0.30	0.17	0.42	0.17	0.59

Kinetics of charge separation. In order to obtain further insight on the mechanisms determining the efficiency of CS in these systems, we introduce a simple model for the calculation of the CS rate constants relying on Marcus' theory and the EG mechanism. This model is based on the following hypothesis (see Annex III, SI, for a detailed description and justification): (i) the evolution of the CS efficiencies across the series of different D-A combinations can be reasonably

evaluated by comparing the very first hopping step of the charge transport from the interface toward the bulk. This is based on the idea that the electron-hole binding energy corresponding to the first CS step is at least two times larger than for the second CS step. Comparing the first CS steps across the series allows for a comparison of the propensity for electrons and holes to escape from the interface. This model is reported hereafter as first-step charge-separation model (FSCS); (ii) the CS rate constants can be calculated separately for holes ($k_{CS\text{-}h}$) and electrons ($k_{CS\text{-}e}$).

The results from the FSCS model calculations are shown in **Figure 10** and Table S7, whereas a detailed analysis based on numerical simulations in the frame of FSCS model is given in Annexes II and III. The results indicate that the $k_{CS\text{-}h}$ / k_{CTSR} and $k_{CS\text{-}e}$ / k_{CTSR} ratios, which provide a pertinent estimation of the charge generation efficiency, increase continuously upon substituting P3HT with POPT and NDI with PDI.

3. Discussion

The present results provide important insights into the impact of the polymer structure and composition on the charge-generation efficiency in BHJ solar cells. Figure 10 summarizes theoretical key parameters and compares these to the experimental photocurrents generated by the 4 model systems. As the photogeneration in these devices is field independent and free charge recombination nearly absent at short circuit (Fig. 2 and S2), the internal quantum efficiency provides a direct measure of the charge generation efficiency. Importantly, the FSCS model parameters as well as the total energy gradient and charge-transfer state recombination rate follow the trends in J_{SC} and *IQE*. Thus, the gradually improved charge generation efficiency observed experimentally can be explained by the joint contribution of the increased steric hindrance at the D-A interface, and the increased energy gradient between the interface and the bulk of the donor and acceptor materials. Both effects decrease k_{CTSR}, and increase $k_{CS\text{-}e,h}$, jointly improving charge generation across the series, as shown in Figure 10. In the following we discuss the complex interplay between structural and electronic properties in detail.

Effect of steric hindrance. The increase in the steric hindrance in our compounds arises from the twisted phenyl groups with respect to the POPT backbone, but also from the strongly non-planar π-backbone in the case of PDI-based acceptor. Both steric effects result in reduced CTSR rate constants in mPOPT-mPDI by roughly three orders of magnitude as compared to mP3HT-mNDI, basically stemming from two effects: (i) the increase in the inter-chain separation results in reduced

electronic couplings between S_0-CT_1 ($HOMO_{donor}$- $LUMO_{acceptor}$) by roughly 5 times. (ii) The CT_1 state energy in POPT-containing D-A interfaces increases when compared to P3HT-containing blends by 0.11 eV. This last effect stems from the increased $HOMO_{donor}$-$LUMO_{acceptor}$ gap at the interface, which increases by the same amount as the corresponding gap deduced from the isolated compounds (bulk), whereas the electron-hole binding energies exhibit minor variations ($\leq$ 0.04 eV, Table 3). The increase in the CT state energy in this case thus stems from increased geometrical distortions at the D-A interface. Therefore, we conclude, in agreement with previous works,[78-79] that *increasing the steric hindrance by means of aromatic (bulky) side groups constitutes an efficient vector for reducing the geminate recombination rates*. It can be expected that these effects contribute importantly to the success of phenyl- or thiophene side chains in donor polymers similar to POPT, such as PTB7-Th, PBDTBDD-Th or in the case of the molecular acceptor ITIC (Figure 1).

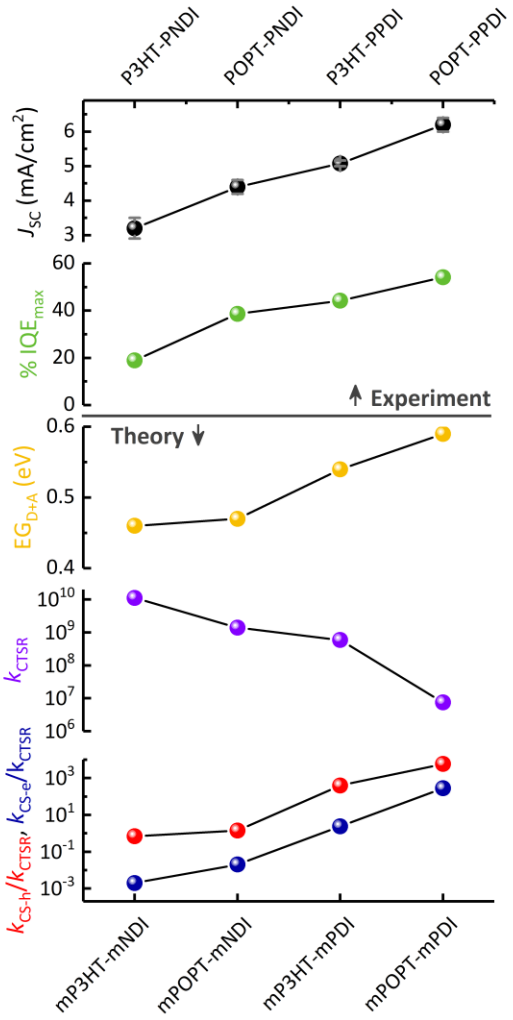

Figure 10. Comparison of experimental parameters (uncertainties derived from device statistics are given in Table S1) of the solar cell systems presented in Figure 2 with key theoretical parameters describing the energy gradient at the D-A interface (EG_{D+A}, Table 3), the charge-transfer state recombination rate (k_{CTSR}, Table 2) and the relative charge generation efficiencies (k_{CS-h} / k_{CTSR} and k_{CS-e} / k_{CTSR} ratios, Table S7) obtained by the FSCS model.

Evolution of the energy gradient. An important observation from Table 3 and Figure 9 is that the total energy gradient values (EG_{D+A}), ranging from 0.45-0.6 eV, are large enough to overcome the e-h binding energy of 0.3 eV, consistent with the field-independent charge generation observed in all D-A blends (Figure S1). The continuous increase in EG among the sample series follows the trend in J_{SC} observed experimentally (Figure 10). However, the driving forces for the hole-drift out of the interface (EG_D = 0.30-0.42 eV) are larger than those of electrons (EG_A = 0.12-0.17 eV). This suggests a larger stabilization for the holes in the donor bulk as compared to the stabilization of the electrons in the acceptor bulk, in agreement with similar results (0.27 eV) for a pentacene:C60 mixture.[80] This disparity in hole- and electron EGs may consequently be an issue

for these systems: while holes could quickly escape from the interface, the electrons would spend more time in the vicinity of the donors, potentially enhancing the CTSR efficiency.

The presence of an EG that pushes charges from the interface to the bulk, has been previously proposed to be the origin for the efficient charge generation in fullerene-containing solar cells.[17-23] Important contributions to EG (up to 0.16 eV) come from the geometrical deformations of the conjugated backbones of the thiophene donors. This finding is consistent with other theoretical studies on P3HT-PCBM systems (0.15 eV [18] and 0.12 eV [23]) or from cyclic voltammetry- and ultraviolet photoelectron spectroscopy (UPS) results, also reporting on an hole energy-level offset of up to 0.15 eV between crystalline and amorphous P3HT phases.[81] These results suggest that the geometrical flexibility of thiophene-based polymers can provide roughly half of the driving force in fighting the e-h binding energy in these systems (≈0.3 eV), thus being beneficial to charge separation through EG mechanisms.

Interestingly, the geometric contribution to the energy gradient of the acceptor-LUMOs is roughly zero (EG_A, Table 3), which could be attributed to the localization of the LUMOs on the rigid NDI and PDI cores (Figure 3). One might expect that increased flexibility of the acceptor polymer π-backbone would lead to larger molecular deformations that increase the energy gradient. However, while this assumption sounds reasonable, other factors seem to be involved. Indeed, test calculations for the geometrical contribution to the energy gradient of donor polymer frontier MOs (hence corresponding to identical geometrical deformations for both orbitals) reveal a much smaller impact on the LUMOs (0.076 eV and 0.015 eV for mP3HT and mPOPT respectively) as compared to the HOMOs (EG_D of 0.150 eV and 0.120 eV, respectively, Table 3). The geometrical flexibility of polymer π-backbones is consequently neither the only factor responsible for the smaller geometrical contribution of the LUMO compared to that of the HOMO, nor the dominant one. Additional effects in this regard may include: (i) first-principles differences between frontier orbitals in these polymers (Figure S5),[18] and/or (ii) the flexibility of the polymer π-backbone may not necessarily guarantee important impact of the geometrical contribution to EG.[82] Nevertheless, the relatively large LUMO-EG found for the flexible P3HT π-backbone (as compared to more rigid NDI- and PDI-based polymers) suggests that non-negligible beneficial effects to EG_A could stem from a more flexible structure. Judiciously designed acceptor blocks and/or linking topology may consequently be needed in order to increase the impact of the geometrical deformations to the acceptor (and donor) energy bending.

As for the DCP contribution at the D-A interface, the largest EG values (0.18 and 0.21 eV) were found for the effect of mPDI on the HOMO energy of mP3HT and mPOPT respectively, whereas mP3HT, mPOPT, and mNDI were found to induce smaller EG values ranging 0.06-0.11 eV (Table S4). We suspect the larger effect of PDI to be due to the increased direct contact between mPDI and the donor polymers: in spite of introducing a larger average intermolecular distance between donor and acceptor backbones (Table S2), mPDI increases the number of short-contacts ranging 3.0 to 3.3 Å (20 and 9 for mP3HT-mPDI and for mP3HT-mNDI respectively).[83]

Cumulative effects increase charge generation efficiency. The results obtained in the framework of the FSCS model indicate that the $k_{CS\text{-}h}$ / k_{CTSR} and $k_{CS\text{-}e}$ / k_{CTSR} ratios provide a pertinent estimation of the charge generation efficiency (Figure 10, Annexes II and III). To understand the origin of this correlation requires to review the cumulative effects that influence the rate constants.

Substituting mNDI with mPDI in acceptor polymers results in increased $k_{CS\text{-}h}$ due to an increased driving force for hole-drift from 0.30 eV to 0.42 eV (EG_D, Table 3), and increased $k_{CS\text{-}e}$ due to the larger electronic couplings (0.010 eV and 0.071 eV respectively, Table S6) for electron-drift away from the interface. On the other hand, replacing mP3HT with mPOPT increases the intramolecular reorganization energy (from 0.219 eV to 0.321 eV respectively, Table S6), and decreases the D-D electronic couplings (0.139 eV and 0.100 eV respectively, Table S6), both effects being slightly detrimental to CS-h. However, the cumulated effect of both substitutions results in increased CS rates (Annex III). The continuous increase in charge generation efficiency upon substituting P3HT with POPT and PNDI with PPDI is thus due to two effects: (i) decrease in k_{CTSR} by roughly 3 orders of magnitude, and (ii) increase of *CS* efficiency by the same degree. The increase in CS / *CTSR* efficiency ratios is more important in the case of PDI-based acceptors, in which both electronic coupling- and driving force (EG) parameters enhance CS efficiency as compared to NDI-based acceptor.

Interfacial versus bulk properties. The discussion so far indicates that efficient charge generation can be achieved by increasing steric bulk and polymer backbone flexibility. However, the drawback of these polymer modifications is their detrimental impact on the charge mobility toward the electrodes. Indeed, increasing the EG by means of increasing polymer π-backbone flexibility is also expected to increase the geometrical disorder in the donor and acceptor bulks, which is detrimental to electron and hole mobilities. Similarly, increasing the steric bulk by means of

aromatic side groups results in decreased electronic couplings and charge transport properties in the bulk of these materials. Structural modifications in order to improve charge generation operate consequently through opposite effects at the interface versus bulk, implying that judicious choices need to be made in order to avoid both detrimental limit cases. This could for instance be achieved by designing polymer chains exhibiting enhanced planarity driven by weak intra-chain hydrogen- or halogen bonds:[84] while favorable planarity could be possible to preserve in the bulk, breaking of H-bonds (halogen-bonds) could occur at the D-A interface, followed by important geometrical deformations. Nevertheless, our results suggest that while both aspects need to be handled with care, *improving interfacial properties should constitute the primary focus as compared to bulk properties*, otherwise good charge mobility handling with small currents would be a less good choice (see also Annex IV, SI). This suggestion is consistent with our results: while the hole mobility of POPT and the electron mobility of PPDI were found to be lower than those of P3HT and PNDI respectively,[63, 65] the former compounds were found to improve charge generation efficiency in BHJ devices.

4. Conclusions

The results presented in this study provide insights in the mechanisms determining the efficiency to charge separation in a series of conjugated polymer D-A heterojunctions. A model based on Marcus' theory is proposed allowing comparative estimations with respect to the CS efficiencies. The results indicate that the experimentally observed improvements in device performance are due to a delicate balance between several opposite factors. The substitution of P3HT and PNDI with POPT and PPDI has two main effects: (i) the geminate donor-acceptor *CTSR* efficiency decreases, an effect mainly due to the decreased electronic couplings, in turn stemming from the enhanced *steric hindrance induced by the side phenyl groups* in POPT and from the distorted π-backbone in PPDI. The extension of the PPDI *LUMO along the orthogonal direction as compared to the donor π-backbone* also contributes to the decreased electronic couplings and CTSR efficiency; (ii) The CS efficiency increases, due to the increase in the driving force for hole drift out of D-A interface. These driving forces appear as *energy gradients at the interface*, in turn stemming from the geometrical deformations of the polymer π-backbones and polarization effects. The *geometrical flexibility of polymer π-backbones* is consequently an important vector for inducing efficient driving force for e-h pair separation. The evolution upon polymer substitutions of both CTSR- and CS efficiencies cumulated together results in increasing k_{CS} / k_{CTSR} ratios, explaining the increased

J_{SC} values observed experimentally. However, the increased disorder at the interface due to the above structural modifications is also suspected to enlarge the density of CT states, with the drawback of negatively impacting the Voc, which seems in line with the experimental results.

We conclude that the maximum strength of intermolecular interactions in these systems correspond to the face-to-face D-A orientation. The present study suggests that the crucial benefit of the face-to-face orientation in these polymer blends is the creation of the necessary driving forces required to repel / force charges away from the D-A interface. The geometrical deformations of polymer π-backbones were found to contribute substantially to the creation of the driving forces in the case of P3HT and POPT, whereas NDI- and PDI-based acceptor polymers lack this contribution due to (i) the localization of their LUMO on the rigid NDI and PDI moieties, and (ii) due to first-principles differences between HOMO and LUMO in polymers, making LUMO energy being less sensitive to the deformation of inter-monomer dihedral angles then HOMO one. These last effects are suspected to induce a detrimental disparity in driving forces for the separation of electrons and holes. Equilibrating the hole- and electron drift rates may thus be a challenge for high efficiency BHJ OPVs.

Our results suggest consequently several guidelines expected to improve charge generation in all polymer BHJ OPVs by:

1. Decreasing the $HOMO_{donor}$-$LUMO_{acceptor}$ overlap: (i) by increasing the steric hindrance at the D-A interface by introducing aromatic side-chains in polymers or by distorting polymer π-backbones; (ii) by reducing spatial overlap between the donor-acceptor π-backbones by favoring π(D) *versus* π(A) space-extensions orthogonal to each other;
2. Increasing the $HOMO_{donor}$-$LUMO_{acceptor}$ energy gap (energy of the CT states)
3. Increasing the distortions at the interface by increasing the geometrical flexibility of polymer π-backbones, ideally by handling as much as possible the potential for both facile deformability (at the D-A interface) and planarization (in the bulk).

Despite the eventual detrimental impact on charge carrier mobilities, these modifications are expected to improve charge generation efficiency, based on the conclusion that among CTSR, CS, and charge transport phenomena, improving the CS efficiency constitutes the key effect. This means that, *in addition* to other target parameters for efficient BHJ OPVs, the synthetic chemist should also and *firstly think CS*.

Acknowledgments. The authors gratefully thank Jean-Luc Bredas (Georgia Tech, Atlanta, GA, USA) for stimulating discussions throughout this work. G.S. gratefully thanks the calculation center of Cergy-Pontoise University for the computing time and support. C.R. thanks the University of Kentucky Vice President for Research and the Department of the Navy, Office of Naval Research (Award No. N00014-16-1-2985) for support. VC thanks the Department of the Navy, Office of Naval Research (Awards Nos. N00014-14-1-0580 and N00014-16-1-2520) for support. MS and DD acknowledge funding by the German Science Foundation through the SPP 1355 "Elementary Processes in Organic Photovoltaics".

Supporting Information. Additional solar cell data, results from TDCF measurements, theoretical results on the POPT geometry, details on the MO energies, geometrical parameters, electronic couplings and energy gradients of the D-A complexes, intramolecular reorganization energies of the pristine compounds, theoretical rate constants for charge recombination and charge separation, Annexes on the POPT geometry optimizations, charge transport on the pristine materials, and charge separation rate constants, experimental and theoretical methods.

REFERENCES

1. Zhao, J.; Li, Y.; Yang, G.; Jiang, K.; Lin, H.; Ade, H.; Ma, W.; Yan, H., Effcient organic solar cells processed from hydrocarbon solvents. *Nature Energy* **2016,** *1* (February 2016), 15027.
2. Bin, H. J.; Zhang, Z. G.; Gao, L.; Chen, S. S.; Zhong, L.; Xue, L. W.; Yang, C.; Li, Y. F., Non-Fullerene Polymer Solar Cells Based on Alkylthio and Fluorine Substituted 2D-Conjugated Polymers Reach 9.5% Efficiency. *Journal of the American Chemical Society* **2016,** *138* (13), 4657-4664.
3. Lin, Y.; Zhao, F.; He, Q.; Huo, L.; Wu, Y.; Parker, T. C.; Ma, W.; Sun, Y.; Wang, C.; Zhu, D.; Heeger, A. J.; Marder, S. R.; Zhan, X., High-Performance Electron Acceptor with Thienyl Side Chains for Organic Photovoltaics. *Journal of the American Chemical Society* **2016,** *138* (14), 4955-4961.
4. Zhao, W. C.; Qian, D. P.; Zhang, S. Q.; Li, S. S.; Inganas, O.; Gao, F.; Hou, J. H., Fullerene-Free Polymer Solar Cells with over 11% Efficiency and Excellent Thermal Stability. *Advanced Materials* **2016,** *28* (23), 4734-4739.
5. Gao, L.; Zhang, Z. G.; Xue, L. W.; Min, J.; Zhang, J. Q.; Wei, Z. X.; Li, Y. F., All-Polymer Solar Cells Based on Absorption-Complementary Polymer Donor and Acceptor with High Power Conversion Efficiency of 8.27%. *Advanced Materials* **2016,** *28* (9), 1884-1890.
6. Hwang, Y.-J.; Courtright, B. A. E.; Ferreira, A. S.; Tolbert, S. H.; Jenekhe, S. A., 7.7% Efficient All-Polymer Solar Cells. *Advanced Materials* **2015,** *27* (31), 4578-4584.
7. Holliday, S.; Ashraf, R. S.; Wadsworth, A.; Baran, D.; Yousaf, S. A.; Nielsen, C. B.; Tan, C. H.; Dimitrov, S. D.; Shang, Z. R.; Gasparini, N.; Alamoudi, M.; Laquai, F.; Brabec, C. J.; Salleo, A.; Durrant, J. R.; McCulloch, I., High-efficiency and air-stable P3HT-based polymer solar cells with a new non-fullerene acceptor. *Nature Communications* **2016,** *7*, 11585.
8. Kim, T.; Kim, J. H.; Kang, T. E.; Lee, C.; Kang, H.; Shin, M.; Wang, C.; Ma, B. W.; Jeong, U.; Kim, T. S.; Kim, B. J., Flexible, highly efficient all-polymer solar cells. *Nature Communications* **2015,** *6*, 8547.
9. Jamieson, F. C.; Domingo, E. B.; McCarthy-Ward, T.; Heeney, M.; Stingelin, N.; Durrant, J. R., Fullerene crystallisation as a key driver of charge separation in polymer/fullerene bulk heterojunction solar cells. *Chemical Science* **2012,** *3* (2), 485-492.
10. Rao, A.; Chow, P. C. Y.; Gelinas, S.; Schlenker, C. W.; Li, C. Z.; Yip, H. L.; Jen, A. K. Y.; Ginger, D. S.; Friend, R. H., The role of spin in the kinetic control of recombination in organic photovoltaics. *Nature* **2013,** *500* (7463), 435-439.
11. Tamura, H.; Burghardt, I., Ultrafast Charge Separation in Organic Photovoltaics Enhanced by Charge Delocalization and Vibronically Hot Exciton Dissociation. *Journal of the American Chemical Society* **2013,** *135* (44), 16364-16367.
12. Tamura, H.; Tsukada, M., Role of intermolecular charge delocalization on electron transport in fullerene aggregates. *Physical Review B* **2012,** *85* (5), 054301.
13. Schubert, M.; Dolfen, D.; Frisch, J.; Roland, S.; Steyrleuthner, R.; Stiller, B.; Chen, Z.; Scherf, U.; Koch, N.; Facchetti, A.; Neher, D., Influence of Aggregation on the Performance of All-Polymer Solar Cells Containing Low-Bandgap Naphthalenediimide Copolymers. *Advanced Energy Materials* **2012,** *2* (3), 369-380.
14. Schubert, M.; Collins, B. A.; Mangold, H.; Howard, I. A.; Schindler, W.; Vandewal, K.; Roland, S.; Behrends, J.; Kraffert, F.; Steyrleuthner, R.; Chen, Z.; Fostiropoulos, K.; Bittl, R.; Salleo, A.; Facchetti, A.; Laquai, F.; Ade, H. W.; Neher, D., Correlated Donor/Acceptor Crystal Orientation Controls Photocurrent Generation in All-Polymer Solar Cells. *Advanced Functional Materials* **2014,** *24* (26), 4068-4081.

15. Sirringhaus, H.; Brown, P. J.; Friend, R. H.; Nielsen, M. M.; Bechgaard, K.; Langeveld-Voss, B. M. W.; Spiering, A. J. H.; Janssen, R. A. J.; Meijer, E. W.; Herwig, P.; de Leeuw, D. M., Two-dimensional charge transport in self-organized, high-mobility conjugated polymers. *Nature* **1999,** *401* (6754), 685-688.
16. Yan, H.; Chen, Z.; Zheng, Y.; Newman, C.; Quinn, J. R.; Dotz, F.; Kastler, M.; Facchetti, A., A high-mobility electron-transporting polymer for printed transistors. *Nature* **2009,** *457* (7230), 679-686.
17. Ishii, H.; Sugiyama, K.; Ito, E.; Seki, K., Energy level alignment and interfacial electronic structures at organic metal and organic organic interfaces. *Advanced Materials* **1999,** *11* (8), 605-685.
18. McMahon, D. P.; Cheung, D. L.; Troisi, A., Why Holes and Electrons Separate So Well in Polymer/Fullerene Photovoltaic Cells. *Journal of Physical Chemistry Letters* **2011,** *2* (21), 2737-2741.
19. Beljonne, D.; Cornil, J.; Muccioli, L.; Zannoni, C.; Bredas, J.-L.; Castet, F., Electronic Processes at Organic-Organic Interfaces: Insight from Modeling and Implications for Opto-electronic Devices. *Chemistry of Materials* **2011,** *23* (3), 591-609.
20. Poelking, C.; Andrienko, D., Design Rules for Organic Donor-Acceptor Heterojunctions: Pathway for Charge Splitting and Detrapping. *Journal of the American Chemical Society* **2015,** *137* (19), 6320-6326.
21. Poelking, C.; Tietze, M.; Elschner, C.; Olthof, S.; Hertel, D.; Baumeier, B.; Wuerthner, F.; Meerholz, K.; Leo, K.; Andrienko, D., Impact of mesoscale order on open-circuit voltage in organic solar cells. *Nature Materials* **2015,** *14* (4), 434-439.
22. Yost, S. R.; Van Voorhis, T., Electrostatic Effects at Organic Semiconductor Interfaces: A Mechanism for "Cold" Exciton Breakup. *Journal of Physical Chemistry C* **2013,** *117* (11), 5617-5625.
23. D'Avino, G.; Mothy, S.; Muccioli, L.; Zannoni, C.; Wang, L.; Cornil, J.; Beljonne, D.; Castet, F., Energetics of Electron-Hole Separation at P3HT/PCBM Heterojunctions. *Journal of Physical Chemistry C* **2013,** *117* (25), 12981-12990.
24. Hou, J. H.; Tan, Z. A.; Yan, Y.; He, Y.; Yang, C.; Li, Y. F., Synthesis and Photovoltaic Properties of Two-Dimensional Conjugated Polythiophenes with Bi(thienylenevinylene) Side Chains. *Journal of the American Chemical Society* **2006,** *128* (14), 4911-4916.
25. Holcombe, T. W.; Norton, J. E.; Rivnay, J.; Woo, C. H.; Goris, L.; Piliego, C.; Griffini, G.; Sellinger, A.; Bredas, J.-L.; Salleo, A.; Frechet, J. M. J., Steric Control of the Donor/Acceptor Interface: Implications in Organic Photovoltaic Charge Generation. *Journal of the American Chemical Society* **2011,** *133* (31), 12106-12114.
26. Huo, L. J.; Zhang, S. Q.; Guo, X.; Xu, F.; Li, Y. F.; Hou, J. H., Replacing Alkoxy Groups with Alkylthienyl Groups: A Feasible Approach To Improve the Properties of Photovoltaic Polymers. *Angewandte Chemie-International Edition* **2011,** *50* (41), 9697-9702.
27. Liao, S. H.; Jhuo, H. J.; Cheng, Y. S.; Chen, S. A., Fullerene Derivative-Doped Zinc Oxide Nanofilm as the Cathode of Inverted Polymer Solar Cells with Low-Bandgap Polymer (PTB7-Th) for High Performance. *Advanced Materials* **2013,** *25* (34), 4766-4771.
28. Yao, H. F.; Ye, L.; Zhang, H.; Li, S. S.; Zhang, S. Q.; Hou, J. H., Molecular Design of Benzodithiophene-Based Organic Photovoltaic Materials. *Chemical Reviews* **2016,** *116* (12), 7397-7457.
29. Ye, L.; Zhang, S. Q.; Huo, L. J.; Zhang, M. J.; Hou, J. H., Molecular Design toward Highly Efficient Photovoltaic Polymers Based on Two-Dimensional Conjugated Benzodithiophene. *Accounts of Chemical Research* **2014,** *47* (5), 1595-1603.

30. Zhang, S. Q.; Ye, L.; Zhao, W. C.; Liu, D. L.; Yao, H. F.; Hou, J. H., Side Chain Selection for Designing Highly Efficient Photovoltaic Polymers with 2D-Conjugated Structure. *Macromolecules* **2014,** *47* (14), 4653-4659.
31. Lin, Y. Z.; Zhao, F. W.; He, Q.; Huo, L. J.; Wu, Y.; Parker, T. C.; Ma, W.; Sun, Y. M.; Wang, C. R.; Zhu, D. B.; Heeger, A. J.; Marder, S. R.; Zhan, X. W., High-Performance Electron Acceptor with Thienyl Side Chains for Organic Photovoltaics. *Journal of the American Chemical Society* **2016,** *138* (14), 4955-4961.
32. Yao, H. F.; Yu, R. N.; Shin, T. J.; Zhang, H.; Zhang, S. Q.; Jang, B.; Uddin, M. A.; Woo, H. Y.; Hou, J. H., A Wide Bandgap Polymer with Strong pi-pi Interaction for Efficient Fullerene-Free Polymer Solar Cells. *Advanced Energy Materials* **2016,** *6* (15).
33. Chen, W.; Zhang, Q., Recent progress in non-fullerene small molecule acceptors in organic solar cells (OSCs). *Journal of Materials Chemistry C* **2017,** *5* (6), 1275-1302.
34. Zhang, Z. G.; Li, Y. F., Side-chain engineering of high-efficiency conjugated polymer photovoltaic materials. *Science China-Chemistry* **2015,** *58* (2), 192-209.
35. Fan, Y. L.; Barlow, S.; Zhang, S. Y.; Lin, B. P.; Marder, S. R., Comparison of 3D non-fullerene acceptors for organic photovoltaics based on naphthalene diimide and perylene diimide-substituted 9,9 '-bifluorenylidene. *Rsc Advances* **2016,** *6* (74), 70493-70500.
36. Hwang, Y. J.; Li, H. Y.; Courtright, B. A. E.; Subramaniyan, S.; Jenekhe, S. A., Nonfullerene Polymer Solar Cells with 8.5% Efficiency Enabled by a New Highly Twisted Electron Acceptor Dimer. *Advanced Materials* **2016,** *28* (1), 124-131.
37. Zhong, H. L.; Wu, C. H.; Li, C. Z.; Carpenter, J.; Chueh, C. C.; Chen, J. Y.; Ade, H.; Jen, A. K. Y., Rigidifying Nonplanar Perylene Diimides by Ring Fusion Toward Geometry-Tunable Acceptors for High-Performance Fullerene-Free Solar Cells. *Advanced Materials* **2016,** *28* (5), 951-958.
38. Zhong, Y.; Trinh, M. T.; Chen, R. S.; Wang, W.; Khlyabich, P. P.; Kumar, B.; Xu, Q. Z.; Nam, C. Y.; Sfeir, M. Y.; Black, C.; Steigerwald, M. L.; Loo, Y. L.; Xiao, S. X.; Ng, F.; Zhu, X. Y.; Nuckolls, C., Efficient Organic Solar Cells with Helical Perylene Diimide Electron Acceptors. *Journal of the American Chemical Society* **2014,** *136* (43), 15215-15221.
39. Duan, Y.; Xu, X.; Yan, H.; Wu, W.; Li, Z.; Peng, Q., Pronounced Effects of a Triazine Core on Photovoltaic Performance–Efficient Organic Solar Cells Enabled by a PDI Trimer-Based Small Molecular Acceptor. *Advanced Materials* **2017,** *29* (7), 1605115.
40. Dou, C.; Long, X.; Ding, Z.; Xie, Z.; Liu, J.; Wang, L., An Electron-Deficient Building Block Based on the B←N Unit: An Electron Acceptor for All-Polymer Solar Cells. *Angewandte Chemie* **2016,** *128* (4), 1458-1462.
41. Deshmukh, K. D.; Prasad, S. K. K.; Chandrasekaran, N.; Liu, A. C. Y.; Gann, E.; Thomsen, L.; Kabra, D.; Hodgkiss, J. M.; McNeill, C. R., Critical Role of Pendant Group Substitution on the Performance of Efficient All-Polymer Solar Cells. *Chemistry of Materials* **2017,** *29* (2), 804-816.
42. Jung, J. W.; Jo, W. H., Low-Bandgap Small Molecules as Non-Fullerene Electron Acceptors Composed of Benzothiadiazole and Diketopyrrolopyrrole for All Organic Solar Cells. *Chemistry of Materials* **2015,** *27* (17), 6038-6043.
43. Lee, W.; Lee, C.; Yu, H.; Kim, D. J.; Wang, C.; Woo, H. Y.; Oh, J. H.; Kim, B. J., Side Chain Optimization of Naphthalenediimide-Bithiophene-Based Polymers to Enhance the Electron Mobility and the Performance in All-Polymer Solar Cells. *Advanced Functional Materials* **2016,** *26* (10), 1543-1553.
44. Li, H. Y.; Earmme, T.; Subramaniyan, S.; Jenekhe, S. A., Bis(Naphthalene Imide)diphenylanthrazolines: A New Class of Electron Acceptors for Efficient Nonfullerene Organic Solar Cells and Applicable to Multiple Donor Polymers. *Advanced Energy Materials* **2015,** *5* (8).

45. Tang, Y. Q.; McNeill, C. R., All-polymer solar cells utilizing low band gap polymers as donor and acceptor. *Journal of Polymer Science Part B-Polymer Physics* **2013,** *51* (6), 403-409.
46. Wu, C. H.; Chueh, C. C.; Xi, Y. Y.; Zhong, H. L.; Gao, G. P.; Wang, Z. H.; Pozzo, L. D.; Wen, T. C.; Jen, A. K. Y., Influence of Molecular Geometry of Perylene Diimide Dimers and Polymers on Bulk Heterojunction Morphology Toward High-Performance Nonfullerene Polymer Solar Cells. *Advanced Functional Materials* **2015,** *25* (33), 5326-5332.
47. Zhang, X.; Li, W. P.; Yao, J. N.; Zhan, C. L., High-Efficiency Nonfullerene Polymer Solar Cell Enabling by Integration of Film-Morphology Optimization, Donor Selection, and Interfacial Engineering. *Acs Applied Materials & Interfaces* **2016,** *8* (24), 15415-15421.
48. Zhong, Y.; Trinh, M. T.; Chen, R. S.; Purdum, G. E.; Khlyabich, P. P.; Sezen, M.; Oh, S.; Zhu, H. M.; Fowler, B.; Zhang, B. Y.; Wang, W.; Nam, C. Y.; Sfeir, M. Y.; Black, C. T.; Steigerwald, M. L.; Loo, Y. L.; Ng, F.; Zhu, X. Y.; Nuckolls, C., Molecular helices as electron acceptors in high-performance bulk heterojunction solar cells. *Nature Communications* **2015,** *6*.
49. Zhou, E.; Cong, J. Z.; Hashimoto, K.; Tajima, K., Control of Miscibility and Aggregation Via the Material Design and Coating Process for High-Performance Polymer Blend Solar Cells. *Advanced Materials* **2013,** *25* (48), 6991-6996.
50. Zhou, N. J.; Lin, H.; Lou, S. J.; Yu, X. G.; Guo, P. J.; Manley, E. F.; Loser, S.; Hartnett, P.; Huang, H.; Wasielewski, M. R.; Chen, L. X.; Chang, R. P. H.; Facchetti, A.; Marks, T. J., Morphology-Performance Relationships in High-Efficiency All-Polymer Solar Cells. *Advanced Energy Materials* **2014,** *4* (3).
51. Cai, Y. H.; Huo, L. J.; Sun, X. B.; Wei, D. H.; Tang, M. S.; Sun, Y. M., High Performance Organic Solar Cells Based on a Twisted Bay-Substituted Tetraphenyl Functionalized Perylenediimide Electron Acceptor. *Advanced Energy Materials* **2015,** *5* (11).
52. Gautam, B. R.; Lee, C.; Younts, R.; Lee, W.; Danilov, E.; Kim, B. J.; Gundogdu, K., Charge Generation Dynamics in Efficient All-Polymer Solar Cells: Influence of Polymer Packing and Morphology. *Acs Applied Materials & Interfaces* **2015,** *7* (50), 27586-27591.
53. Hwang, Y. J.; Li, H. Y.; Courtright, B. A. E.; Subramaniyan, S.; Jenekhe, S. A., Nonfullerene Polymer Solar Cells with 8.5% Efficiency Enabled by a New Highly Twisted Electron Acceptor Dimer. *Advanced Materials* **2016,** *28* (1), 124-+.
54. Jung, J.; Lee, W.; Lee, C.; Ahn, H.; Kim, B. J., Controlling Molecular Orientation of Naphthalenediimide-Based Polymer Acceptors for High Performance All-Polymer Solar Cells. *Advanced Energy Materials* **2016,** *6* (15).
55. Li, M. M.; Liu, Y. T.; Ni, W.; Liu, F.; Feng, H. R.; Zhang, Y. M.; Liu, T. T.; Zhang, H. T.; Wan, X. J.; Kan, B.; Zhang, Q.; Russell, T. P.; Chen, Y. S., A simple small molecule as an acceptor for fullerene-free organic solar cells with efficiency near 8%. *Journal of Materials Chemistry A* **2016,** *4* (27), 10409-10413.
56. Lin, Y. Z.; Wang, J. Y.; Zhang, Z. G.; Bai, H. T.; Li, Y. F.; Zhu, D. B.; Zhan, X. W., An Electron Acceptor Challenging Fullerenes for Efficient Polymer Solar Cells. *Advanced Materials* **2015,** *27* (7), 1170-1174.
57. Lin, Y. Z.; Zhang, Z. G.; Bai, H. T.; Wang, J. Y.; Yao, Y. H.; Li, Y. F.; Zhu, D. B.; Zhan, X. W., High-performance fullerene-free polymer solar cells with 6.31% efficiency. *Energy & Environmental Science* **2015,** *8* (2), 610-616.
58. Liu, F.; Zhou, Z. C.; Zhang, C.; Vergote, T.; Fan, H. J.; Liu, F.; Zhu, X. Z., A Thieno 3,4-b thiophene-Based Non-fullerene Electron Acceptor for High-Performance Bulk-Heterojunction Organic Solar Cells. *Journal of the American Chemical Society* **2016,** *138* (48), 15523-15526.
59. Richter, T. V.; Braun, C. H.; Link, S.; Scheuble, M.; Crossland, E. J. W.; Stelzl, F.; Wurfel, U.; Ludwigs, S., Regioregular Polythiophenes with Alkylthiophene Side Chains. *Macromolecules* **2012,** *45* (14), 5782-5788.

60. Wang, X. F.; Lv, L.; Li, L. L.; Chen, Y. S.; Zhang, K.; Chen, H. R.; Dong, H. L.; Huang, J. S.; Shen, G. Z.; Yang, Z.; Huang, H., High-Performance All-Polymer Photoresponse Devices Based on Acceptor-Acceptor Conjugated Polymers. *Advanced Functional Materials* **2016,** *26* (34), 6306-6315.
61. Xiao, B.; Ding, G. D.; Tan, Z. A.; Zhou, E. J., A comparison of n-type copolymers based on cyclopentadithiophene and naphthalene diimide/perylene diimides for all-polymer solar cell applications. *Polymer Chemistry* **2015,** *6* (43), 7594-7602.
62. Steyrleuthner, R.; Di Pietro, R.; Collins, B. A.; Polzer, F.; Himmelberger, S.; Schubert, M.; Chen, Z. H.; Zhang, S. M.; Salleo, A.; Ade, H.; Facchetti, A.; Neher, D., The Role of Regioregularity, Crystallinity, and Chain Orientation on Electron Transport in a High-Mobility n-Type Copolymer. *Journal of the American Chemical Society* **2014,** *136* (11), 4245-4256.
63. Holcombe, T. W.; Woo, C. H.; Kavulak, D. F. J.; Thompson, B. C.; Frechet, J. M. J., All-Polymer Photovoltaic Devices of Poly(3-(4-n-octyl)-phenylthiophene) from Grignard Metathesis (GRIM) Polymerization. *Journal of the American Chemical Society* **2009,** *131* (40), 14160-1.
64. Andersson, M. R.; Selse, D.; Berggren, M.; Jarvinen, H.; Hjertberg, T.; Inganas, O.; Wennerstrom, O.; Osterholm, J. E., Regioselective Polymerization of 3-(4-Octylphenyl)Thiophene With FeCl3. *Macromolecules* **1994,** *27* (22), 6503-6506.
65. Chen, Z.; Zheng, Y.; Yan, H.; Facchetti, A., Naphthalenedicarboximide- vs Perylenedicarboximide-Based Copolymers. Synthesis and Semiconducting Properties in Bottom-Gate N-Channel Organic Transistors. *Journal of the American Chemical Society* **2009,** *131* (1), 8-9.
66. Andersson, M. R.; Berggren, M.; Inganas, O.; Gustafsson, G.; Gustafssoncarlberg, J. C.; Selse, D.; Hjertberg, T.; Wennerstrom, O., Electroluminescence From Substituted Poly(Thiophenes) - From Blue to Near-Infrared. *Macromolecules* **1995,** *28* (22), 7525-7529.
67. Verploegen, E.; Mondal, R.; Bettinger, C. J.; Sok, S.; Toney, M. F.; Bao, Z., Effects of Thermal Annealing Upon the Morphology of Polymer-Fullerene Blends. *Advanced Functional Materials* **2010,** *20* (20), 3519-3529.
68. Rivnay, J.; Toney, M. F.; Zheng, Y.; Kauvar, I. V.; Chen, Z.; Wagner, V.; Facchetti, A.; Salleo, A., Unconventional Face-On Texture and Exceptional In-Plane Order of a High Mobility n-Type Polymer. *Advanced Materials* **2010,** *22* (39), 4359-4363.
69. We note that we are aware of the well-known deficiencies of B3LYP to describe CT excited states, so that the above agreement is due to wrong reasons. However, we are interested only on the trends across the series of the DA complexes, which seems to be well reproduced in the frame of this study.
70. Hush, N. S., Intervalence-Transfer Absorption. Part 2. Theoretical Considerations and Spectroscopic Data. *Progress in Inorganic Chemistry* **1967,** *8*, 391.
71. Hush, N. S., Homogeneous and heterogeneous optical and thermal electron transfer. *Electrochimica Acta* **1968,** *13* (5), 1005-1023.
72. Gould, I. R.; Noukakis, D.; Gomezjahn, L.; Young, R. H.; Goodman, J. L.; Farid, S., Radiative and Nonradiative Electron-Transfer in Contact Radical-Ion Pairs. *Chemical Physics* **1993,** *176* (2-3), 439-456.
73. At first sight the above observation seems at odds with the quite efficient P3HT exciton-quenching. However, the exciton dissociation is expected to happen through several possible channels, corresponding to several unoccupied acceptor orbitals suitably situated with respect to donor (acceptor) S1 level (Figure 5), thus making the exciton dissociation proceeding in the Marcus normal region. On the other hand, CR is supposed to proceed deep in Marcus inverted region, involving Gibbs free energies of the order of 1.0-1.2 eV (Table 3). This last effect is

expected to negatively impact the CR rates, importantly overcompensating for the larger CR electronic couplings. .
74. Marcus, R. A., On the Theory of Oxidation- Reduction Reactions Involving Electron Transfer. I. *J. Chem. Phys.* **1956,** *24*, 966.
75. Marcus, R. A., Electron transfer reactions in chemistry. Theory and experiment. *Rev. Mod. Phys.* **1993,** *65*, 599.
76. Marcus, R. A.; Sutin, N., Electron transfers in chemistry and biology. *Biochim. Biophys. Acta* **1985,** *811*, 265.
77. **We remember that, instead of energy contributions stemming from the interaction with- or between induced dipoles, the term "polarization" here includes (for historical reasons) principally contributions from electrostatic interactions.**
78. Xiao, X.; Wei, G. D.; Wang, S. Y.; Zimmerman, J. D.; Renshaw, C. K.; Thompson, M. E.; Forrest, S. R., Small-Molecule Photovoltaics Based on Functionalized Squaraine Donor Blends. *Advanced Materials* **2012,** *24* (15), 1956-1960.
79. Zimmerman, J. D.; Xiao, X.; Renshaw, C. K.; Wang, S. Y.; Diev, V. V.; Thompson, M. E.; Forrest, S. R., Independent Control of Bulk and Interfacial Morphologies of Small Molecular Weight Organic Heterojunction Solar Cells. *Nano Letters* **2012,** *12* (8), 4366-4371.
80. Ryno, S. M.; Risko, C.; Bredas, J.-L., Impact of Molecular Orientation and Packing Density on Electronic Polarization in the Bulk and at Surfaces of Organic Semiconductors. *ACS applied materials & interfaces* **2016,** *8* (22), 14053-62.
81. Sweetnam, S.; Graham, K. R.; Ndjawa, G. O. N.; Heumueller, T.; Bartelt, J. A.; Burke, T. M.; Li, W.; You, W.; Amassian, A.; McGehee, M. D., Characterization of the Polymer Energy Landscape in Polymer:Fullerene Bulk Heterojunctions with Pure and Mixed Phases. *Journal of the American Chemical Society* **2014,** *136* (40), 14078-14088.
82. Troisi, A.; Shaw, A., Very Large π^- Conjugation Despite Strong Nonplanarity: A Path for Designing New Semiconducting Polymers. *J. Phys. Chem. Lett* **2016,** *7*, 4689−4694.
83. Attempts to correlate this difference with dipole moments were unsuccessful, as large variations in total dipole moments or in their z-component are not consistent with the trends of EGD or EGA across the series (Table S4). The increasing quadrupolar moments (Q) between mNDI and mPDI (-708 and -996 Debye-Å respectively) do correlate with the increased polarization-EGs from 0.08 eV to roughly 0.20 eV (Table S3). However, larger Q variation in the case of donors as compared to acceptors (delta-Q ~370 Debye-Å and ~290 Debye-Å respectively) seems to have no- or out-of-trend effect on the variation of the polarization-induced EGA. Indeed, mPOPT induces smaller LUMO-EG to mNDI as compared to mPDI (0.07 and 0.11 eV respectively), whereas the mPOPT quadrupolar z-component is larger in the mPOPT-mNDI complexe as compared to mPOPT-mPDI one (-979 and -922 Debye-Å respectively).
84. Conboy, G.; Spencer, H. J.; Angioni, E.; Kanibolotsky, A. L.; Findlay, N. J.; Coles, S. J.; Wilson, C.; Pitak, M. B.; Risko, C.; Coropceanu, V.; Bredas, J. L.; Skabara, P. J., To bend or not to bend - are heteroatom interactions within conjugated molecules effective in dictating conformation and planarity? *Materials Horizons* **2016,** *3* (4), 333-339.

Understanding photocurrent generation at the molecular level is one of the biggest challenges in organic solar cell research. By performing an experimental and theoretical in-depth study we are able to correlate molecular structure with charge generation efficiency in prototypical polymer solar cells. Our results provide clear structure-property relationships that will help to design a new generation of non-fullerene acceptors.

Organic Heterojunctions

Gjergji Sini,[#,*] Marcel Schubert,[#,*] Chad Risko,* Steffen Roland, Olivia P. Lee, Zhihua Chen, Thomas V. Richter, Daniel Dolfen, Veaceslav Coropceanu, Sabine Ludwigs, Ullrich Scherf, Antonio Facchetti, Jean M. J. Fréchet, Dieter Neher*

On the Molecular Origin of Charge Separation at the Donor-Acceptor Interface

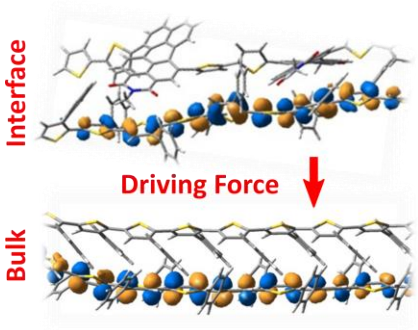

Supporting Information

On the Molecular Origin of Charge Separation at the Donor-Acceptor Interface

Gjergji Sini,[#,] Marcel Schubert,[#,]* Chad Risko,* Steffen Roland, Olivia P. Lee, Zhihua Chen, Thomas V. Richter, Daniel Dolfen, Veaceslav Coropceanu,[b] Sabine Ludwigs, Ullrich Scherf, Antonio Facchetti, Jean M. J. Fréchet, Dieter Neher**

I- Figures

II- Tables

III- Annexes

IV- Methods

I- Figures

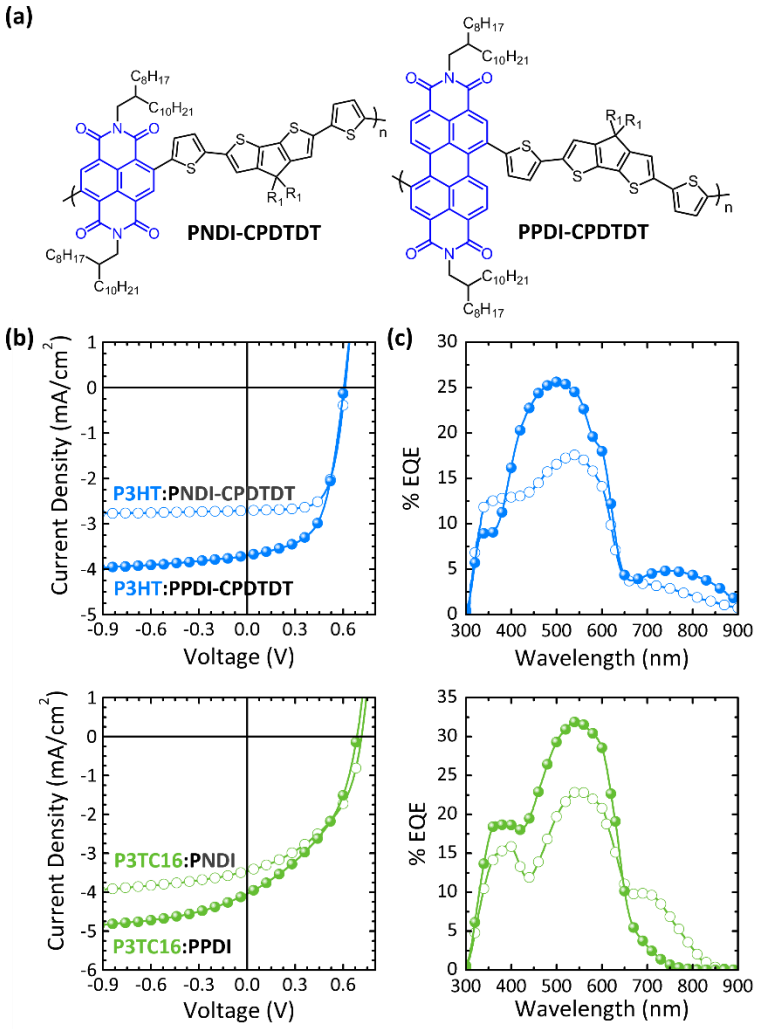

Figure S1. (a) Additional acceptor polymers PNDI-CPDTDT and PPDI-CPDTDT, which comprise the same backbone modification as PNDI and PPDI, namely the replacement of NDI by larger and bulkier PDI. R_1=ethylhexyl **(b)** and **(c)** Solar cell characteristics of P3HT (blue, top) blended with (PNDI-CPDTDT, open symbols) and (PPDI-CPDTDT, closed symbols) and P3TC16 (green, bottom) combined with (PNDI, open symbols) and (PPDI, closed symbols) **(b)** Current Density-Voltage characteristics under AM 1.5 G illumination and **(c)** EQE spectra for all 4 combinations.

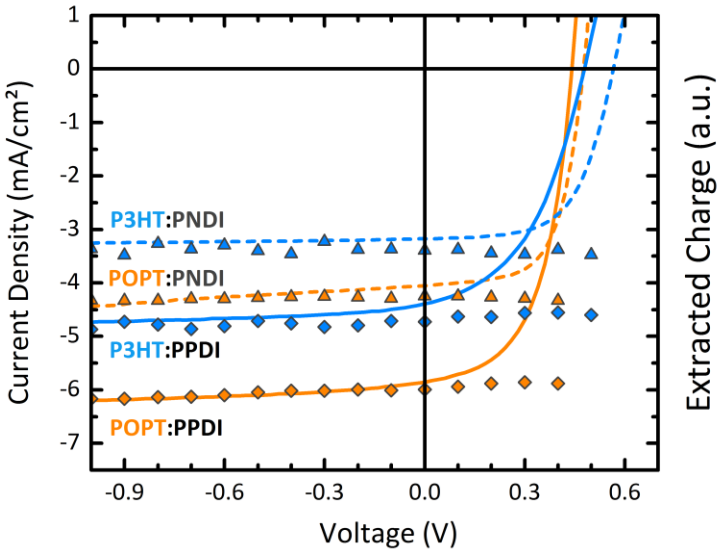

Figure S2. Photogenerated free charge measured as a function of applied voltage with time-delayed collection field (TDCF) experiments (symbols). Also shown are JV-characteristics from devices (solid and dashed lines) produced in parallel to the TDCF sample revealing the same trends as shown in the Figure 2 of main text.

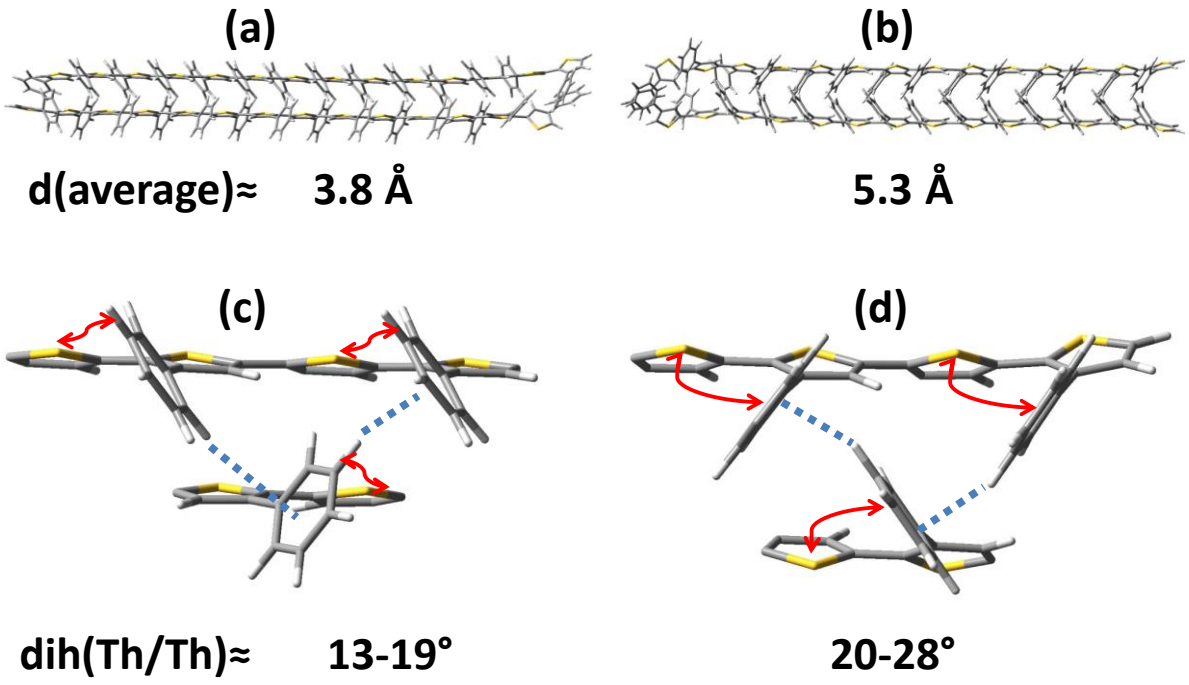

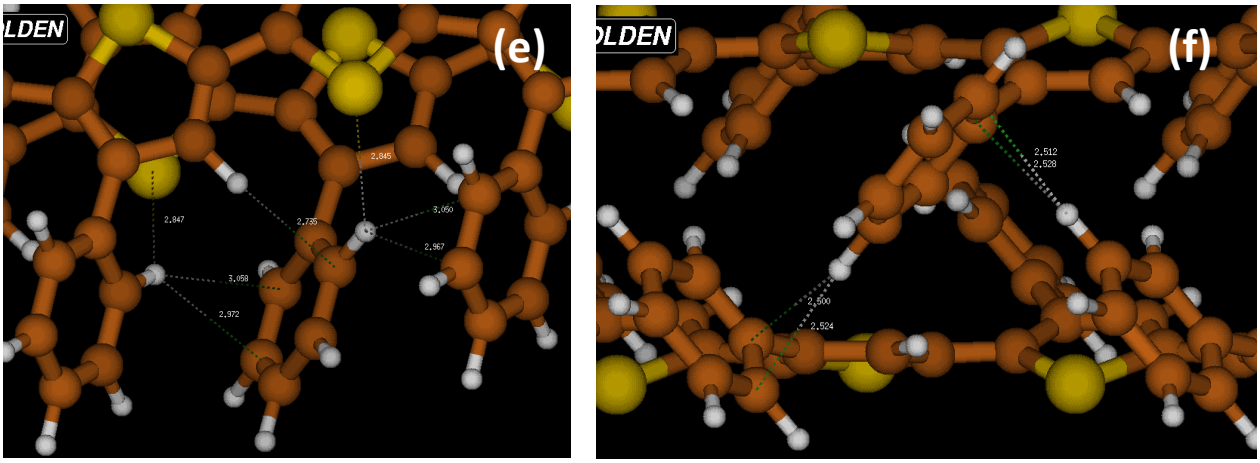

Figure S3. Side view of **(a)** dimPOPT1 and **(b)** dimPOPT3 model dimers optimized at the ωB97XD/6-31G* level of theory. **(c)** and **(d)** are magnified views of (a) and (b), respectively. The interactions between the phenyl and adjacent thiophene groups are highlighted by the red arrows. Note that these repulsion interactions seem to impose small thiophene-thiophene dihedral angles in the case of dimPOPT1, but larger ones in the case of dimPOPT3. (Ph)C-H...π(Ph) interactions (2.5 to 3.1 Å) between phenyl groups of adjacent molecules are highlighted by the blue dashed lines. **(e)** Side view of dimPOPT1 and **(f)** dimPOPT3 model dimers optimized at the ωB97XD/6-31G* level of theory. In both cases, selected short contacts corresponding to H-bonds are highlighted. Images obtained with MOLDEN software.[1]

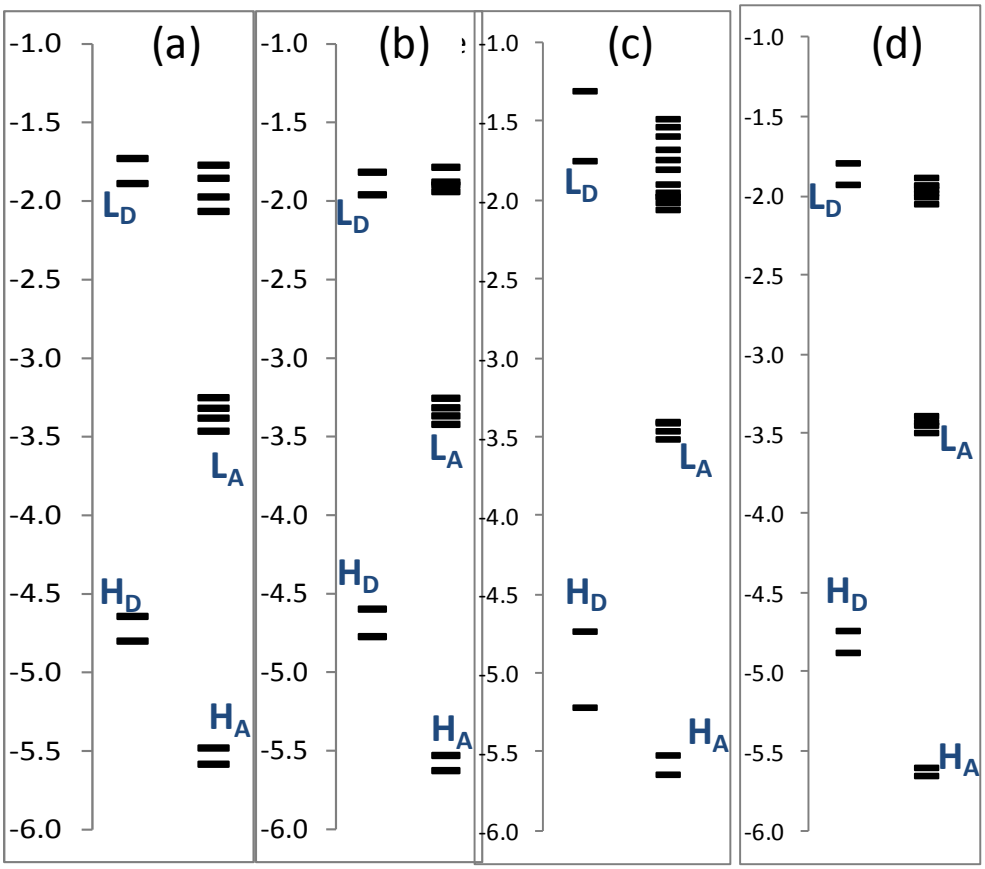

Figure S4. (a-d) Molecular orbital energy diagrams for donor and acceptor oligomers in the geometries obtained from the D-A complexes mP3HT-mNDI, mPOPT-mNDI, mP3HT-mPDI and mPOPT-mPDI, respectively, as calculated at the B3LYP/6-31G*//ωB97XD/6-31G* level of theory. Average values over three isomers for each complex are used.

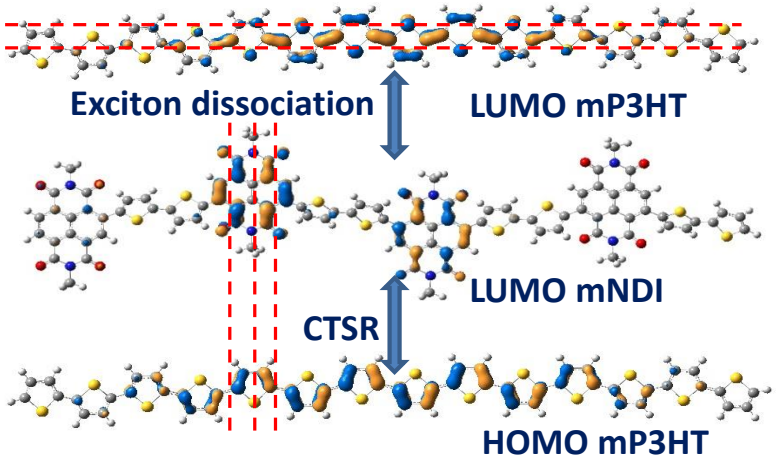

Figure S5. Pictorial representations of the HOMO and LUMO of mP3HT, and LUMO of mNDI. The red dashed lines highlight the orientation of the principal nodal planes on each of these orbitals. The LUMO of P3HT corresponds to the bonding (in-phase) combination between monomer-LUMOs as compared to the antibonding (out-of-phase) combination between monomer-HOMOs in the polymer HOMO. As a rule of thumb, the impact of geometrical deformations on the energy of the bonding orbitals is smaller as compared to antibonding ones, thus giving a possible explanation for the smaller sensitivity of LUMO of P3HT and POPT to dihedral-angle deformations as compared to the corresponding HOMOs.

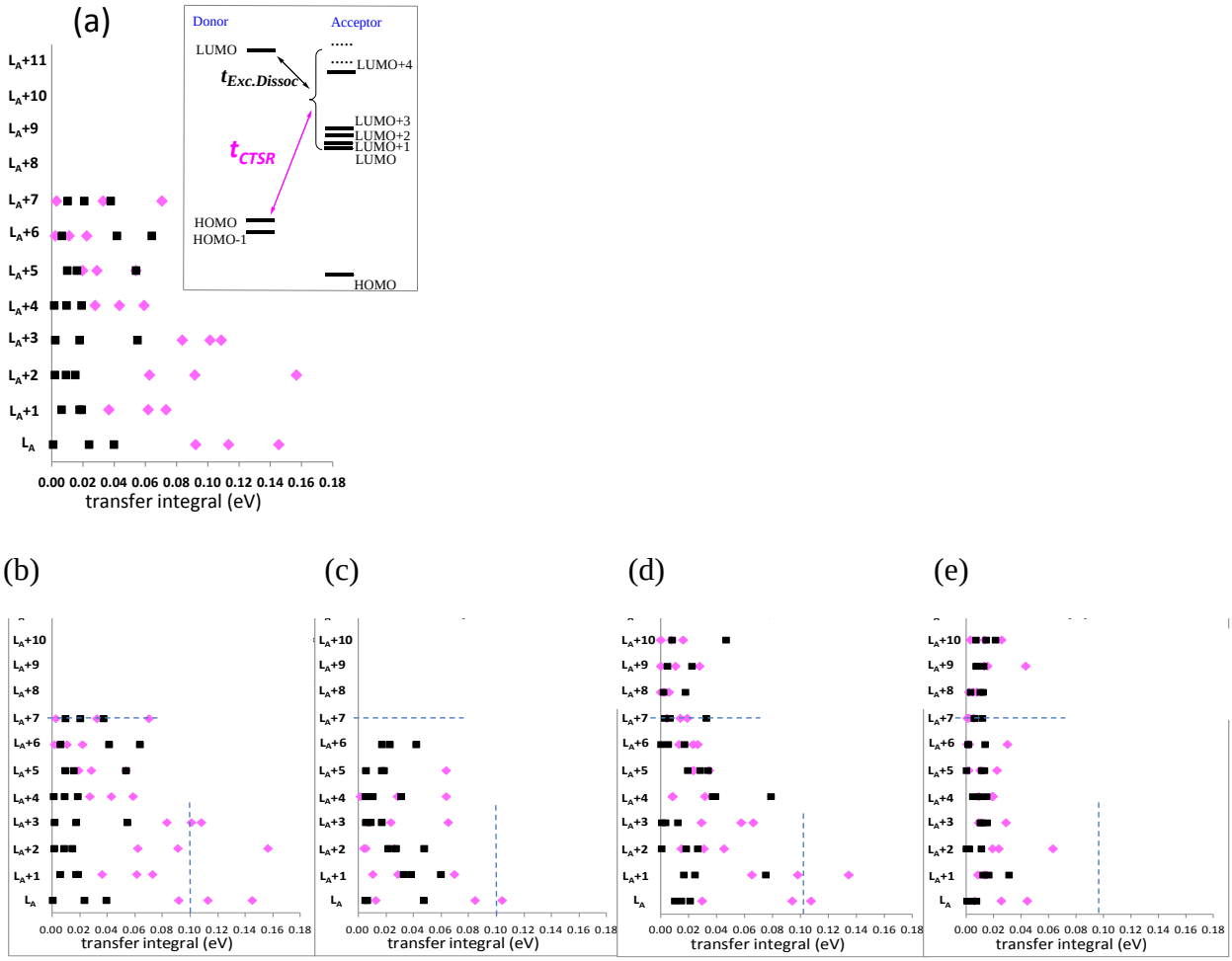

Figure S6. Electronic couplings (eV) corresponding to **(a)** the ensemble of twelve complexes (three isomers times four DA combinations), calculated between $HOMO_{donor}$ and $LUMO_{donor}$ with the acceptor LUMO through LUMO+n, as indicated in the inset. **(c-f)** similar to (a) in the case of mP3HT-mNDI, mPOPT-mNDI, mP3HT-mPDI, and mPOPT-mPDI, respectively. The blue dashed lines are guides for the eye. The electronic couplings were calculated at the B3LYP/6-31G*//ωB97XD/6-31G* level.

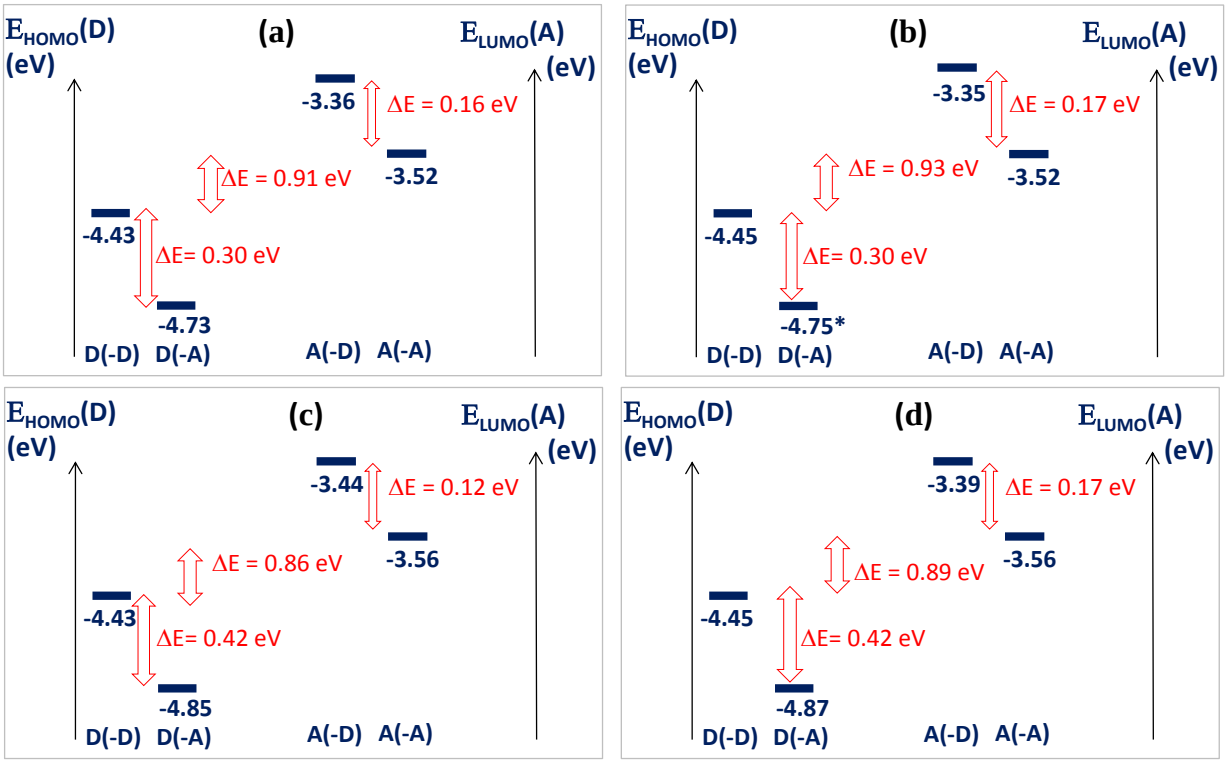

Figure S7. Energy diagrams showing the built-in energy gradient (eV, B3LYP/6-31G*) near and at the D-A interface for $HOMO_{donor}$ and $LUMO_{acceptor}$ corresponding to **(a)** mP3HT-mNDI **(b)** mPOPT-mNDI **(c)** mP3HT-mPDI and **(d)** mPOPT-mPDI. Each value in the figure corresponds to the average out of three values (*average of two values for the D(-A) energy in b).

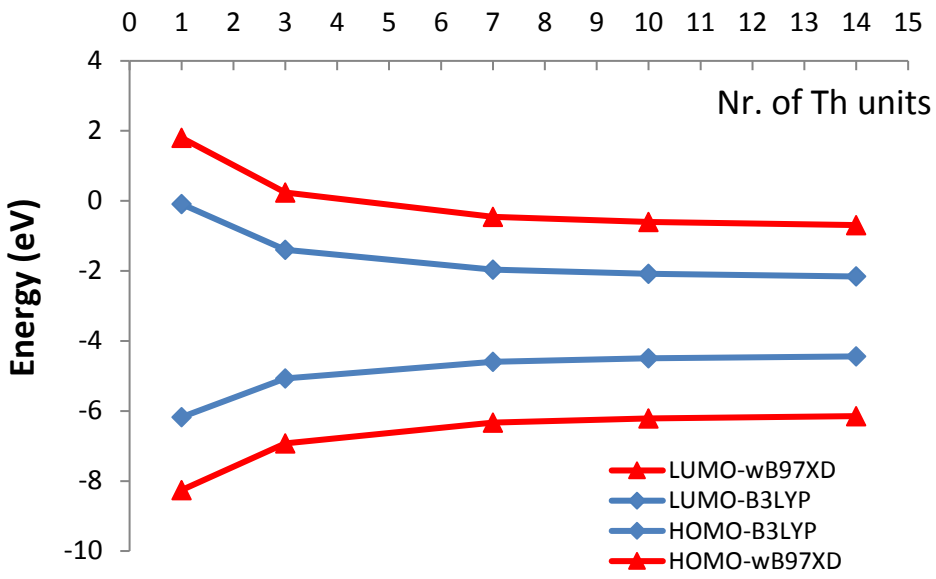

Figure S8. Evolution of HOMO energy (eV) of thiophene-based oligomers as a function of number of monomer units as calculated at the B3LYP/6-31G** level of theory.

II- Tables

Table S1. Device performances for BHJ OPVs prepared by combining P3HT and POPT donor polymers with the acceptor polymers PNDI and PPDI. Device parameters are stated as mean value with the standard deviation given in parentheses. J_{SC}=Short circuit current density, V_{OC}=open circuit voltage, *FF*=fill factor, *PCE*=power conversion efficiency, N_{dev}=number of solar cells tested, IQE_{max}=maximum internal quantum efficiency.

	J_{SC}	V_{OC}	*FF*	*PCE*	N_{dev}	IQE_{max}
	mA/cm^2	V	%	%		%
P3HT-PNDI	-3.2 (0.3)	0.563 (0.007)	65 (4)	1.2 (0.1)	22	19
POPT-PNDI	-4.4 (0.2)	0.492 (0.007)	61 (3)	1.36 (0.08)	28	39
P3HT-PPDI	-5.08 (0.08)	0.50 (0.02)	52 (5)	1.4 (0.2)	8	44
POPT-PPDI	-6.2 (0.2)	0.447 (0.004)	50 (4)	1.42 (0.09)	22	54

Table S2. Average donor-acceptor distances (Å) between the π-conjugated backbones calculated at the geometries optimized at the ωB97XD/6-31G* level in "gas phase". Three isomers are optimized for each D-A complex and their average distance (Å) is given in the last column. Standard deviations are given in parentheses. Each distance in the table corresponds to the average value of the shortest distances between any atom of one π-conjugated chain with the π-conjugated backbone of the other chain.

	Isomer-1	Isomer-2	Isomer-3	Average
mP3HT-mNDI	3.60 (0.24)	3.58 (0.20)	3.53 (0.14)	3.57 (0.19)
mPOPT-mNDI	3.62 (0.18)	3.73 (0.35)	-	3.68 (0.27)
mP3HT-mPDI	3.66 (0.36)	3.68 (0.35)	3.65 (0.27)	3.66 (0.33)
mPOPT-mPDI	3.87 (0.46)	3.79 (0.42)	3.74 (0.33)	3.80 (0.40)

Table S3. Electronic couplings (eV) between $HOMO_{donor}$-$LUMO_{acceptor}$ (t_{H-L}) and between states (t_{MH}, t_{TD}) calculated at the B3LYP/6-31G*//ωB97XD/6-31G* level in "gas phase".

	t_{H-L} [a]	t_{MH} [b]	t_{TD} [c]
mP3HT-mNDI	0.117	0.091	0.099
mPOPT-mNDI	0.079	0.086	0.059
mP3HT-mPDI	0.077	0.092	0.075
mPOPT-mPDI	0.025	0.019	0.028

[a]Average over three values corresponding to three isomers for each complex. [b]Calculated according to Mulliken-Hush theory[2-4] [c]Calculated as a weighted sum of couplings between orbitals contributing to $S_0 \rightarrow CT_1$ excitation. The weighting coefficients are taken from TD-B3LYP calculations on donor-acceptor complexes.

Table S4. Energy gradients for the donor (EG_D) and acceptor (EG_D) (eV), dipole moments (Debye) and quadrupole moments (Debye- Å), of model mP3HT, mPOPT, mNDI, and mPDI polymers. The values (B3LYP/6-31G*//ωB97XD/6-31G* level) corresponding to complex geometries are averages over six complexes for each polymer.

	HOMO			
	mP3HT(mNDI)[a]	mPOPT(mNDI) [a]	mP3HT(mPDI) [a]	mPOPT(mPDI) [a]
EG_D	0.08	0.08	0.21	0.18
	LUMO			
	mNDI(mP3HT) [a]	mPDI(mP3HT) [a]	mNDI(mPOPT) [a]	mPDI(mPOPT) [a]
EG_A	0.11	0.06	0.07	0.11

		mP3HT	mPOPT	mNDI	mPDI
Dipolar	isolated-Total	2.8	2.3	5.7	2.0
	isolated-z axes	0.0	0.2	0.7	-0.5
	in complex-z axes [b]	1.3	1.9	0.9	0.7
Quadrupolar	isolated-Total	-532	-866	-756	-995
	isolated-zz component	-530	-873	-759	-994
	in complex-Total	-538	-909	-708	-996
	in complex- zz component	-588	-945	-726	-1019

[a] mP3HT(mNDI) means EG of HOMO-mP3HT induced by mNDI. [b]Average of absolute values.

Table S5. Electronic couplings ($t_{h/e}$ in eV, B3LYP/6-31G*//wB97XD/6-31G* level in "gas phase") between donor-HOMOs, and the Gibbs free energies used during the calculation of rate constants for the hole- and electron drifts from the interface to the bulk (Table 2 in the main text).

		$t_{h/e}$	$\Delta G°$
holes	mP3HT /mNDI	0.07	-0.15
	mP3HT /mPDI	0.07	-0.25
	mPOPT /mNDI	0.05	-0.15
	mPOPT /mPDI	0.05	-0.25
electrons	mNDI / mP3HT	0.005	-0.11
	mNDI /mPOPT	0.005	-0.11
	mPDI / mP3HT	0.035	-0.08
	mPDI /mPOPT	0.035	-0.11

Table S6. Intra-molecular reorganization energies ($\lambda_{h/e}$) and transfer integrals ($t_{h/e}$) for holes (between the donor-HOMO orbitals) and electrons (between the acceptor-LUMO orbitals) of pristine compounds, as calculated at the B3LYP/6-31G*//ωB97XD/6-31G* level in "gas phase". All values are in eV.

	$\lambda_{h/e}$	$t_{h/e}$
mP3HT	0.219(h)	0.139(h)
mPOPT	0.321(h)	0.100(0.001)(h)
mNDI	0.084(e)	0.010(e)
mPDI	0.080(e)	0.071(e)

Table S7. Estimated hole- ($k_{CS\text{-}h}$) and electron ($k_{CS\text{-}e}$) rate-constants (s^{-1}), calculated in the frame of Marcus theory. Intra-molecular reorganization energies ($\lambda_{h/e}$), transfer integrals ($t_{h/e}$)[a] for holes and electrons of pristine compounds are taken from Table S6. EG and $E_{bind}^{e\text{-}h}$ values for the Gibbs free energy are taken from Table 3,[a] and a constant value of 0.4 eV was considered for the solvent reorganization energy. The values in parentheses are calculated by arbitrary setting the electronic couplings for holes and electrons to a constant value of 0.070 eV.[b]

	$k_{CS\text{-}h}$	$k_{CS\text{-}e}$	$k_{CS\text{-}h}$ / $k_{CS\text{-}e}$	k_{CTSR}	$k_{CS\text{-}h}$ / k_{CTSR}	$k_{CS\text{-}e}$ / k_{CTSR}
mP3HT-mNDI	$8.3x10^{9}$	$2.5x10^{7}$	330 (1.7)	$1.1x10^{10}$	0.7 (0.7)	$2x10^{-3}$ (0.4)
mPOPT-mNDI	$1.9x10^{9}$	$2.3x10^{7}$	84 (0.8)	$1.4x10^{9}$	1.4 (2.7)	$2x10^{-2}$ (3.2)
mP3HT-mPDI	$2.3x10^{11}$	$1.4x10^{9}$	168 (42)	$5.9x10^{8}$	4 $x10^{2}$ (400)	2.4 (9.5)
mPOPT-mPDI	$4.5x10^{10}$	2.1 $x10^{9}$	22 (11)	$7.5x10^{6}$	6 $x10^{3}$ (1.2 $x10^{4}$)	$2.8x10^{2}$ (1107)

[a] We consider that the geometrical EG values calculated in this work constitute an upper limit, so that half of the geometrical contribution on EG values in Table 3 is considered for the Gibbs free energy (ΔG°). Additionally, we arbitrary consider only 2/3 of ΔG° for the first charge-hopping step. Test calculations by varying the ΔG° indicate that the general trends remain practically unaffected. The electronic couplings considered in these estimations are arbitrary taken as half of those calculated for the non-deformed oligomers (Table S6), based on the idea that the geometrical deformations are not identical in the first two layers near the interface. See Table S4 for the individual EG and electronic coupling values. [b] In order to allow for a clearer comparison with k_{CTSR}, this value is arbitrary taken equal to the average electronic coupling corresponding to CTSR (Table 2).

Table S8. Device preparation details for the solar cells shown in Figure 2 of the main text.

	D/A weight ratio	Total conc.	Solvent mixture	Spin Coating	Drying/Annealing
P3HT:PNDI	1:0.75	40 g/l	p-Xyl:CN (1:1)	2000 rpm, 5 sec.	1 min at 200°C
P3HT:PPDI	2:1	33 g/l	p-Xyl:CN (1:1)	1500 rpm, 5 sec.	1 min. at 180°C
POPT:PNDI	2:1	15 g/l	DCB:CN (4:1)	1000 rpm, 5sec.	2 min. at 80°C
POPT:PPDI	1:1.5	24 g/l	DCB:CN (9:1)	1200 rpm, 5sec.	Dried at room Temp./ 10 min. at 150°C

III- Annexes

Annex I. Geometry of POPT

The geometry of POPT presents particularly interesting features. The phenyl groups of the isolated oligomer (Figure 1) adopt twisted positions with respect to the thiophenes, with dihedral angles of roughly 48° (in the central part of the 14-mer). Notably, studies of the solid-state characteristics of POPT by Anderson and co-workers[5] reveal that as-cast POPT presents a blue-shifted (by 0.46 eV) absorption maximum when compared to thermally- or chloroform-vapour annealed films (Table 1). Based on X-ray and spectroscopic evidence,[6] the POPT geometry was suggested to present two major conformers, one in which the phenyl (Ph) groups remain almost parallel (in-plane) to the thiophene (Th) backbone, corresponding to average inter-planar distance of 3.8 Å, and one with more or less orthogonal Ph-Th dihedral angles, corresponding to inter-planar distance of 5.1 Å. Our efforts to obtain such conformers for the isolated molecules were unsuccessful. In the following, bulk effects will be shown to be the origin of the two conformers observed experimentally.

Geometry optimizations on mPOPT dimers result in three conformers that differ in the inter-planar distances: 3.8 Å, 4.6 Å, and 5.3 Å, reported hereafter as dimPOPT1, dimPOPT2, and dim-POPT3; dimPOPT1 and dimPOPT3 are shown in Figure S3 a-b. The major difference between these dimers comes from the Th-Th dihedral angles, being respectively 13° to 19° and 20° to 28° in dimPOPT1 and dimPOPT3. This difference is found to correlate with two possible orientations of the Ph groups with respect to the adjacent Th groups (Figure S3 c-d). In the case of dimPOPT1, the orientation of the Ph groups in each monomer tends to impose small Th-Th dihedral angles (Figure S3 c), thus resulting in a "flat" POPT backbone and a shorter inter-molecular distance (3.8 Å). Large twisting of the phenyl groups by roughly 90° is observed in dimPOPT3 as compared to dimPOPT1 (Figure S3 d), which in turn results in a much larger inter-molecular distance (5.3 Å). Very good agreement is therefore obtained with the inter-planar distances of 3.8 Å and 5.1 Å observed experimentally in POPT,[6] which is also seen when one compares the energy of the long wavelength absorptions: the low-energy transitions computed by TDDFT for dimPOPT1 and dimPOPT3 were found to be 2.09 eV and 2.29 eV (Table 1), respectively, values that are in good qualitative agreement with experiment, 2.09 eV and 2.56 eV, respectively.[7] DimPOPT2 corresponds to mixed arrangements of Th-Th dihedral angles and Ph/Th orientations, one

monomer of the dimer being similar to dimPOPT1, the second monomer similar to dimPOPT3, thus resulting in intermediate inter-planar distance of 4.6 Å.

In all dimPOPT isomers, the dominant intermolecular interactions are (Ph)C-H...π(Ph) hydrogen bonds between phenyl groups of adjacent polymers (2.5 to 3.1 Å, Figure S3 e-f). The difference between the three isomers is thus due to a delicate balance between the C-H...π short contacts, Ph-S steric hindrance, the conjugation efficiency on the molecular backbones, and the extent of dispersion interactions among the main conjugated backbones. Anderson et al.[7] reported that irreversible change in color and an absorption redshift is obtained after thermal or vapour annealing spin-coated POPT, suggesting that dimPOPT1 type isomers (3.8 Å, "flat" backbone, absorption at 2.09 eV) should be more stable as compared to dim-POPT3 (5.3 Å, more twisted backbone, absorption at 2.29 eV). Interestingly, the Th-Th dihedral angles in the isolated mPOPT model compound (38-43°) are larger as compared to both dimPOPT3 (20-28°) and dimPOPT1 (13-19°). This suggests that the as-cast POPT isomer is formed without intramolecular Ph *versus* Th rearrangements (dimPOPT3), whereas thermal or vapour annealing results in tilting of Ph-Th orientation (Figure S3), reduction of the Th-Th dihedral angles, reduction of the inter-planar distances, and an overall strengthening of the intermolecular interactions (dimPOPT1).

Annex II. **Charge transport properties of model polymers**

As a means to compare the evolution of the CS efficiency in these systems we compare the internal reorganization energies ($\lambda_{h/e}$) and the electronic couplings ($t_{h/e}$) corresponding to the hole- and electron transfer in donor and acceptor compounds. These results are collected in Table S6. The increased reorganization energy and the decreased electronic coupling for mPOPT as compared to mP3HT suggest decreased hole-transfer efficiency in the former. The possible presence of two isomers in the case of POPT, should additionally support the conclusion for larger hole mobility in the case of P3HT. As for the acceptors, improved electron transfer rates can be deduced for the mPDI as compared to mNDI (Table S6). While transport properties in the bulk of these materials could not be reduced to the electronic couplings calculated here, we note however that both theoretical results (concerning donors and acceptors) are not in line with the experimental results indicating similar hole mobilities for P3HT and POPT,[8] and electron mobilities by 10 times larger for the NDI based systems.[9] It is worth noting that the smaller LUMO-LUMO couplings found in

the case of mNDI are not due to a random intermolecular geometry. Indeed, a detailed analysis of dimer geometries reveal the presence of efficient hydrogen bonds (~2.42 Å) between the NDI-oxygen atoms and the C-H bonds of adjacent thiophene rings, imposing a slight parallel displacement between the two monomers, obviously corresponding to a phase mismatch between adjacent LUMOs. A possible explanation on the better transport properties in the NDI-based polymers has been given in terms of very large polymer molar mass, making possible sharing of polymer chains between adjacent crystallites. The much smaller PDI-based polymer mass[9] as compared to NDI may importantly impact the packing and the electron mobility. Additionally, the electronic couplings presented in Table S6 correspond to a static picture and totally ignore: (i) the non-local electron-phonon couplings, probably resulting in increased hopping rates, and (ii) the disorder effect, which we speculate to be less important in the much regular and planar NDI-based polymers. Similarly, we speculate that smaller degree of disorder should be observed in the POPT as compared to P3HT, due to the stronger intermolecular mixing and H-bond interactions between the phenyl groups (Figure S3), probably resulting in reduced freedom for along-chain and transversal displacements, hence in improved hole mobility.

Annex III. **Charge Separation rate estimations. First-Step Charge Separation model (FSCS)**

It is worth noting that the bulk charge-transport efficiency is a long-distance (hundreds of nm) property, thus strongly depending on the disorder, regioregularity, polymer molecular mass, and other properties. However, the energy gradient discussed in this section may happen in a very limited number of π-stacked polymer layers. The "bulk" properties discussed in the last subsections may consequently feed a reasonable model for discussing the CS trends between different D-A combinations.

In order to obtain further insight on the CS trends in these systems, we propose a simplistic model for the calculation of the CS rate constants relying on Marcus' theory[10-12] and the EG mechanism. This model, reported hereafter as first step charge separation (FSCS) model, is based on the following hypothesis:

1- *The trend in the CS efficiencies can be reasonably estimated by comparing the first step of the charge drifts from the interface toward the bulks*. This is based on (i) previous results

reporting on space extension of the energy gradient (bending) limited to only few (roughly three) layers near the D-A interface[13-14]; (ii) the assumption that hole- and electron jumps corresponding to the first step of the charge drifts from the interface toward the bulks constitute the determining step of charge-separation. This assumption can be justified by two observations: firstly, the geometrical deformations and the direct-contact polarization (DCP) appear principally on the interface donor- and acceptor layers, and much less on the few following ones;[15] secondly, the e-h binding energy and the CTSR efficiency become smaller after the first jumps due to the increased e-h separation.

2- *The CS rate constants can be calculated separately for holes (CS-h) and electrons (CS-e).* This is based on the hypothesis that the first hopping steps of electrons and holes toward the respective bulks need not occur simultaneously. This hypothesis is easier to conceive in the limit case of very different electron-*versus*-hole first-step hopping-rates. Indeed, a first-step electron escape from the Coulomb potential was found to be the rate-limiting process for free carrier generation in the case of small molecule:C60 planar heterojunction, due to the faster electron drift by 5 orders of magnitude as compared to the hole drift.[16]

Different limitations of this model include the following (eventually among others): (i) the exact values of long-range polarizations (LRP) are ignored in the EG estimations. However, the EG values used in the first step CS model (FSCS) model being relative ones, calculated as differences between **adjacent** layers, the contribution from the LRP energy is assumed to roughly cancel out (see "Methods" section below). Test calculations over a range of values for the medium reorganization energy and the Gibbs free energy show that the trends across the four D-A combinations remain globally unaffected. (ii) We also ignore any eventual charge delocalization over different π-stacked layers and contribution of the build-up electric field generated by the electrodes. These estimations aim consequently to provide some insight on the contributions to the CS process stemming from the molecular level only.

The results are shown in Table S7. One global observation is that the rate constants for the hole-drift out of the interface ($k_{CS\text{-}h}$, first hopping step) are larger than those of electrons ($k_{CS\text{-}e}$). The much smaller $k_{CS\text{-}e}$ values for mNDI based D-A combinations (roughly 330 times smaller than $k_{CS\text{-}h}$) are mainly due to the small LUMO-LUMO coupling in mNDI (0.005 eV, Table S5). While arbitrary setting all HOMO-HOMO and LUMO-LUMO couplings to the same value results in

roughly similar $k_{CS\text{-}h}$ and $k_{CS\text{-}e}$ values for mP3HT-mNDI and mPOPT-mNDI, this ratio still remains larger than one order of magnitude in the case of mPDI (11-42 times, values in parenthesis in Table S7). This is due to the larger driving force (EG_D = 0.25 eV, Table S5) induced by mPDI to donor-HOMOs, whereas the EG_A values for acceptor-LUMOs range are much smaller (0.08-0.11 eV, Table S5). The large $k_{CS\text{-}h}$ / $k_{CS\text{-}e}$ ratio may consequently be an issue for these systems: while holes could quickly escape from the interface, the electrons would spend more time in the vicinity of the donors, probably enhancing the CTSR efficiency. PDI-based systems seem to be prone to this issue to a larger extent as compared to NDI-based ones. Equilibrating the hole- and electron drift rates may thus be a challenge for high efficiency BHJ OPVs.

Replacing NDI with PDI in acceptor polymers seems to induce only positive effects with-respect-to hole and electron drifts. While both oligomers have similar intramolecular reorganization energies (0.084 eV and 0.080 eV respectively), the $k_{CS\text{-}e}$ increases importantly in the case of mPOPT-mPDI (from $2.5x10^7$ s^{-1} to $2.1x10^9$ s^{-1} respectively, Table S7) due to increased LUMO-LUMO coupling (0.005 and 0.035 eV respectively, Table S5). We remember that replacing NDI with PDI also results in decrease of electronic couplings for theCTSR (Table 2) and in increased driving force (EG, Table 3) for hole drift out of the interface. PDI seems consequently to positively contribute to charge generation by enhancing CS and reducing CTSR.

Replacing P3HT with POPT increases the intramolecular reorganization energy (from 0.219 eV to 0.321 eV respectively, Table S6), and decreases both D-A and D-D electronic couplings (Table 3 and Table S6). These evolutions are detrimental to CTSR, which is the desirable effect, but are also detrimental to CS. These opposite evolutions are thus reflected in the oscillating $k_{CS\text{-}h}$ values across different D-A combinations, decreasing for mPOPT-based combinations as compared to mP3HT ones. Nevertheless, the $k_{CS\text{-}h}$ values globally increase from mP3HT-mNDI to mPOPT-mPDI (from $8.3x10^9$ s^{-1} to $4.5x10^{10}$ s^{-1} respectively, Table S7), reaching a maximum of $2.3x10^{11}$ s^{-1} in the case of mP3HT-mPDI.

We finally discuss the $k_{CS\text{-}h}$ / k_{CTSR} and $k_{CS\text{-}e}$ / k_{CTSR} ratios (Table S7), which provide a pertinent estimation on the evolution of the charge generation efficiency upon substituting P3HT with POPT and NDI with PDI. We firstly focus on the mP3HT-mPDI, exhibiting the smallest k_{CS} / k_{CTSR} values for both holes and electrons. In order to avoid confusion coming from different approximations, we arbitrarily consider identical HOMO-HOMO and LUMO-LUMO couplings of 0.07 eV (half

of the largest electronic coupling corresponding to mP3HT. See Table S7 for explanations). The resulting $k_{CS\text{-}h}$ / k_{CTSR} and $k_{CS\text{-}e}$ / k_{CTSR} ratios of roughly 0.7 and 0.4 respectively suggest only a slight advantage for the CTSR efficiency, which seems in line with the 70% / 30% CTSR/CS ratio found experimentally.

Across the series of different D-A combinations, these k_{CS} / k_{CTSR} ratios are found to increase continuously, which is due to two effects: (i) decrease in k_{CTSR} by roughly 3 orders of magnitude, and (ii) increase of k_{CS} in the same sense by roughly 2 orders of magnitude. The increase in k_{CS} / k_{CTSR} ratios is more important in the case of PDI-based acceptors, in which both electronic coupling- and driving force (EG) parameters enhance CS efficiency as compared to NDI-based acceptor. The collective effect of reduced CTSR- and increased CS efficiencies results in improved charge generation, which is in line with the increased J_{SC} observed experimentally.

Annex IV. ***CS versus CTSR efficiencies: Impact of donor-acceptor orientation.***

Due to the complex anisotropic molecular structure of conjugated polymers it can be expected that charge generation is affected in part by the relative molecular orientation of donor and acceptor polymers. A correlation between the relative orientation of crystalline domains and the photocurrent in P3HT:NDI blends recently indicated improved charge generation in the case of face-to-face crystal orientation,[17] which has been also reported to be the favorable orientation in other material blends. [18-22] Here we try to obtain more insight in the impact of this orientation on the efficiencies of exciton dissociation, CTSR and CS. To this aim, we recall that the k_{CTSR} and k_{CS} estimations in our study were performed by pushing the face-to-face orientation to its maximum efficiency ("cofacial" D-A overlap). This orientation was found to correspond to maximum $HOMO_{donor}$-$LUMO_{acceptor}$ couplings, hence maximum CTSR efficiency, but also to substantial $HOMO_{donor}$ and $LUMO_{acceptor}$ energy gradients (EG_D and EG_A), both effects stemming from the strong interfacial π-π stacking interactions.

One can reasonably suppose that tilting the D/A relative orientation from face-to-face to edge-to-face orientation would result in vanishing small $HOMO_{donor}$-$LUMO_{acceptor}$ couplings and EGs, due to vanishing π-π stacking interactions. We suggest that, despite the decreasing CTSR efficiency in the edge-to-face orientation, the vanishing driving force for CS constitutes the dominant effect, hence being detrimental for the charge generation. This scenario seems to corroborate with the experimental evidence on NDI-P3HT based BHJ OPVs where despite a high exciton dissociation

efficiency (photoluminescence quenching above 90%) in both–face-to-face and edge-to-face–orientation, only the former yielded significant J_{SC}.[17] Given that the CTSR efficiency can only decrease from face-to-face toward edge-to-face rearrangement, *the marginal current generation in the edge-to-face orientation can only reflect the vanishing driving force for CS in this D-A orientation*. Accordingly, *the energy gradient stemming from the interfacial geometrical deformations and polarizations constitutes the dominant benefit generated by the face-to-face D-A orientation* in these BHJ polymer blends.

IV- Methods

1. Device Preparation and Materials

P3HT (Sepiolid P200 from BASF) was purchased from Rieke Metals with a molecular weight of M_n = 17,500 g/mol. POPT and P3TC15 were provided by Prof. Fréchet (University of California, Berkeley) and Prof. Sabine Ludwigs (University of Stuttgart, Germany), respectively, with M_n=45,000 g/mol for POPT and M_w=55.000 g/mol (PDI = 2.0) for P3TC16. The acceptor polymers PNDI and PPDI both were provided by Flexterra Corporation with molecular weights of Mn = 26,200 g/mol and Mn = 16,000 g/mol, respectively. All four D/A systems had been independently optimized and the recipes and preparation routines are summed up in **Table S8**. The solvents that were used are: p-Xylene (p-Xyl), 1-Chloronaphthalene (CN) and 1,2-Dichlorobenzene. We note that the efficiencies presented here comprise the highest reported so far for each material combination. The synthesis of P3TC16 is described in Richter et al.[23]

Synthesis of PNDI-CPDTDT and PPDI-CPDTDT [24-25]

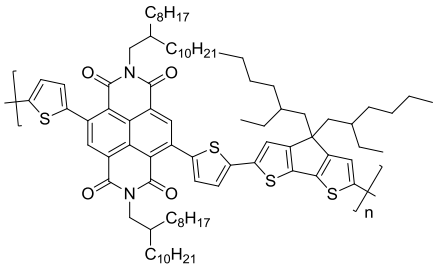

PNDI-CPDTDT

Scheme S1

Poly[N,N'-bis(2-octyldodecyl)-2,6-(bis(2-thienyl)naphthalene-1,4,5,8-tetracarboxydiimide-5,5''-diyl]-*alt*-[4,4-bis(2-ethylhexyl)-4H-cyclopenta[1,2-b:5,4-b']dithiophene-2,6-diyl] **PNDI-CPDTDT**

NDI Monomer

The synthesis of the NDI monomer starts from commercially available naphthalene dianhydride. In the first step dibromination is carried out with bromine in fuming sulfuric acid and iodine as catalyst. The reaction temperature is kept at 30°C to prevent tribromination. The dibrominated product is almost quantitatively obtained, but as a mixture of 2,6-dibromonaphthalene-1,4,5,8-

tetracarboxydianhydride and 2,7-dibromonaphthalene-1,4,5,8-tetracarboxydianhydride. Because of the very low solubility the separation is done after the next step. In the next step the dianhydride is transferred into the diimide by reaction with the alkylamine, in this case 2-octyldodecylamine. The desired 2,6-regioisomer of the dibromonaphthalene diimide can be isolated by column chromatography in a yield of 45%.

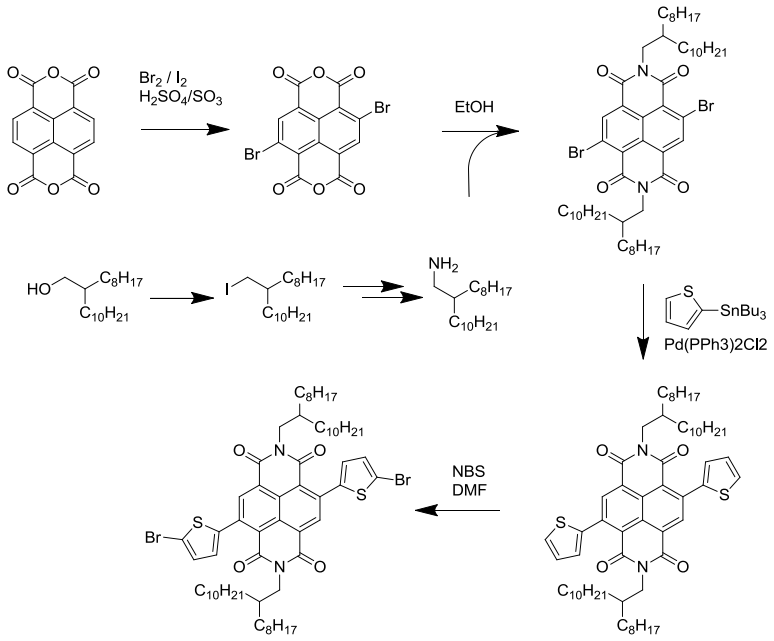

Scheme S2

Next, a Stille type coupling with 2-tributylstannylthiophene is performed. This reaction can be carried out with a yield of 90%. After bromination with NBS, the NDI monomer is obtained.

Copolymer PNDI-CPDTDT

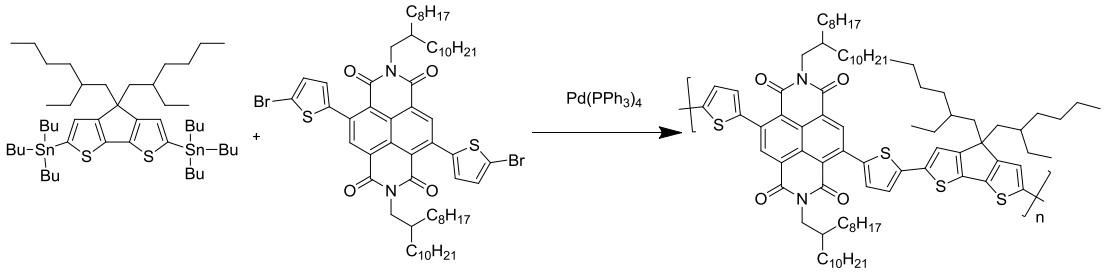

Scheme S3

The copolymer **PNDI-CPDTDT** is synthesized in a Stille-type coupling in toluene at 110°C (3 days). After standard workup and precipitation into cold methanol the polymer is Soxhlet-extracted with methanol, acetone, ethyl acetate, and finally chloroform. The chloroform fraction was precipitated again into cold methanol and analyzed by SEC, TGA, DSC and NMR.

In a Schlenk tube, 813 mg (0,826 mmol) of the NDI monomer are mixed with 5mol% $Pd(PPh_3)_4$ and 1 eq. of the distannylated CPDT (810 mg, 0,826 mmol). After careful exchange of air by argon 15 mL of toluene and 3 mL of DMF are added and the mixture stirred for 3 days at 110°C. The reaction was stopped by addition of 2N aqueous hydrochloric acid and diluted with chloroform. The organic phase was washed each 3 times with aqueous 2N hydrochloric acid, aqueous saturated $NaHCO_3$ solution, and aqueous, saturated EDTA solution. The polymer solution was concentrated and precipitated into cold methanol. Next, the solid polymer was Soxhlet-extracted with methanol, acetone, ethyl acetate, and finally chloroform. The chloroform fraction was precipitated again into cold methanol. Yield: 630 mg (60 %, chloroform fraction).

GPC ($CHCl_3$): M_n = 23,100 g/mol, M_w = 32,200 g/mol, PDI = 1.39

^{1}H-NMR (600 MHz, $C_2D_2Cl_4$, 298 K): δ [ppm] = 8.86 (s, HNaph); 7.41 (m, HCPDT); 4.14 (s, CH_2); 2.05 (s, CH); 1.5 – 0.7 (m, CH_3).

^{13}C-{^{1}H}-NMR: (151 MHz, $C_2D_2Cl_4$, 298 K): δ [ppm] = 162.6; 159.2; 141.7; 140.9; 139.9; 136.3; 132.1; 127.8; 125.5; 122.1; 54.8; 45.4; 44.1; 36.8; 35.9; 35.8; 35.7; 34.7; 34.6; 34.4; 32.3; 32.2; 32.1; 31.9; 31.8; 30.3; 30.2; 30.1; 29.9; 29.8; (3x) 29.7; (2x) 29.6; (2x) 29.5; (2x) 29.3; 29.2; 29.0; 28.9; 28.8; 27.8; 27.7; 27.6; 27.5; 26.9; 26.7; 26.6; 23.1; 23.0; 22.9; (2x) 22.8; 22.7; 22.5; (2x) 14.3; 14.2; (2x) 14.1; 14.0; 13.9; (2x) 11.0; 10.9; 10.8; 10,7; 10.6.

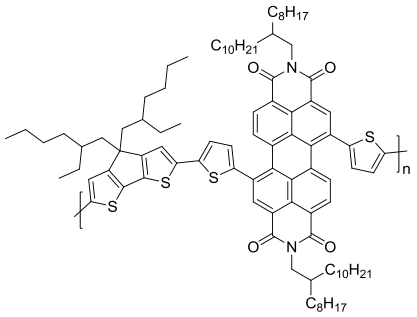

PPDI-CPDTDT

Scheme S4

Poly[N,N'-bis(2-octyldodecyl)-1,7-(bis(2-thienyl)perylene-3,4,9,10-tetracarboxydiimide-5',5''-diyl]-alt-[4,4-bis(2-ethylhexyl)-4H-cyclopenta[1,2-b:5,4-b']dithiophene-2,6-diyl] **PPDI-CPDTDT**

PDI Monomer

The synthesis of the corresponding PDI monomer starts with a dibromination of commercially available perylene dianhydride. When the reaction temperature is kept at 85°C in sulfuric acid as solvent a double bromination can selectively be performed. The reaction is not regioselective. The desired 1,7-dibromoperylene dianhydride is produced in a ratio of 70% besides 1,6-dibromperylene dianhydride. The separation is not done at this stage of the synthesis; therefore, the conversion to the diimide is done with the crude product.

The conversion of the dianhydride into the diimide is carried out as described for the NDI monomer. Nucleophilic aromatic substitution of the amine at the aromatic bromides is an unfavorable side reaction which leads to strongly colored by-products. So, the product can only be obtained in a yield of 35%, but still as a mixture of 1,7- and 1,6-dibromo PDI. After Stille-type coupling with the stannylated thiophene and bromination with NBS the PDI monomer can finally be separated into the regioisomers.

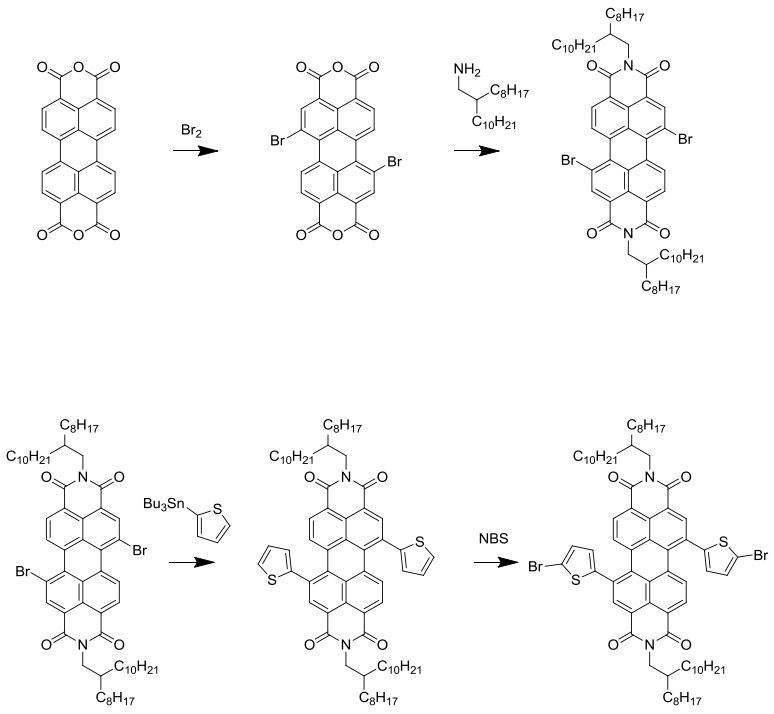

Scheme S5

Copolymer PPDI-CPDTDT

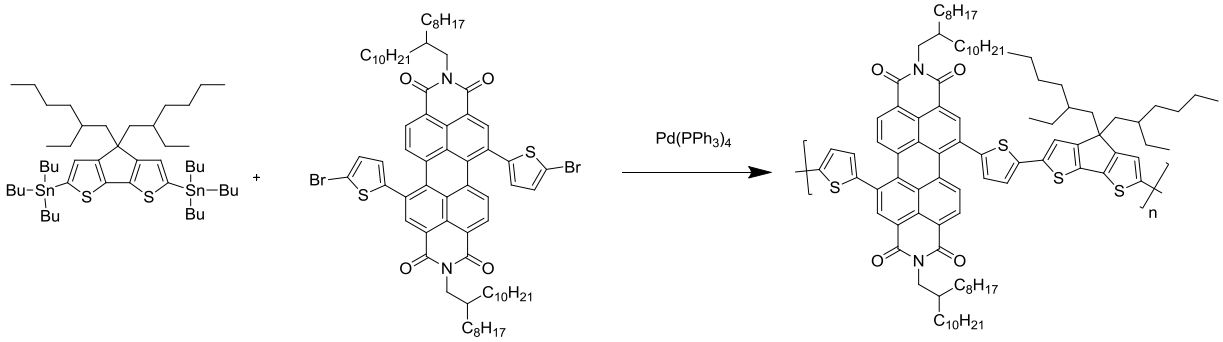

Scheme S6

The copolymer synthesis is done as described for **PNDI-CPDTDT**:

In a Schlenk tube, 800 mg (0,393 mmol) of the PDI monomer are mixed with 5mol% $Pd(PPh_3)_4$ and 1 eq. of the distannylated CPDT (385 mg, 0,393 mmol). Yield: 478 mg (79%, chloroform fraction).

GPC ($CHCl_3$): M_n = 13,000 g/mol, M_w = 20,000 g/mol, PDI = 1.5

^{1}H-NMR (600 MHz, $C_2D_2Cl_4$, 298 K) : δ [ppm] = 8.71 (m, HPer); 8.42 (m, HPer); 8.31(m, HPer); 7.28; 7.23; 7.13 (m, HCPDT); 4.10 (m, CH_2); 2.00 (m, CH_2); 1.89 (m, CH_2); 1.26; 1.06; 0.76; 0.69 (m, CH_2), 0.85 (m, CH_3)

Current-voltage measurements

Standardized illumination was realized with a sun simulator (Newport) calibrated to the AM1.5G spectrum with an intensity of 100 mW/cm^2. Current-Voltage characteristics were measured with a Keithley 2400 source meter.

Absorption

The presented absorption spectra are measured with an Varian Cary 5000 UV-Vis_NIR spectrometer.

External quantum efficiency measurements

Light of a 100 Watt Osram XBO lamp is focused into a monochromator (LOT-Oriel) and mechanically chopped to get trigger signal for the lock-in amplifier (EG&G Princton Applied Resarch Model 5302) which measures the current via a 50Ω resistor. Light source calibration is done by a UV enhanced Silicon photodiode calibrated by Newport (Newport 818-UV).

Internal Quantum efficiencies

IQE spectra were obtained by dividing the EQE spectra by the internal absorption of the solar cell devices (measured with an integrating sphere on the actual solar cells or on separate glass substrates processed in parallel to the solar cell devices), where the absorption was calculated by assuming that light passes the active layer twice.

Time-delayed collection field (TDCF) experiments

Pulsed excitation from a diode pumped, Q-switched Nd:YAG laser (NT242, EKSPLA) with 6 ns pulse duration and 500 Hz repetition rate was used to generate charges in the device. A pulse generator (Agilent 81150A) was used to apply a pre- and collection bias in combination with a home-built amplifier. During the pre bias charges are generated and after a shortest delay of 10 ns

extracted by the collection bias to determine the generation of charges in dependence of the pre bias. [26] To probe recombination behavior the delay can be increased up to several µs. The current through the samples was measured via a 50 Ω resistor and recorded with an oscilloscope (Yokogawa DL9140). The pulse generator was triggered with a fast photodiode (EOT, ET-2030TTL). Laser intensity is measured with a photodiode and an Ophir Vega Power Meter.

2. Computational Methods

An oligomer approach is used to mimic the polymer properties. Compared to more recent high-performance co-polymers, the set of polymers used here has a relatively small molecular size and low structural complexity. This allows us to perform geometry optimizations on dimers (D-D and A-A) and donor-acceptor complexes (D-A) at the DFT level with so far unprecedented molecular size and details. The model polymers are noted mP3HT, mPOPT, mNDI, and mPDI, with m- standing for "model". Given the size of the donor-acceptor monomer units, the oligomers used in the study consisted of four repeat units, while the thiophene homopolymers were represented by 14-unit oligomers (Scheme S7); this gives an effective conjugation length of 28 double bonds in the acceptor systems and 28 double bonds in the thiophene structures. Figure S8 shows almost constant energy of the highest occupied molecular orbital (HOMO) and lowest unoccupied molecular orbital (LUMO) energies with increasing number of thiophene monomer units from 10 to 14 in mP3HT, suggesting that this chain-length is sufficient to obtain size-saturated frontier orbital energies. In order to reduce the computational costs, the solubilizing alkyl chains are represented by methyl groups.

Geometries of donor-acceptor (D-A) complexes – consisting of one donor oligomer (D, a thiophene homopolymer) and one acceptor oligomer (A, a donor-acceptor co-oligomer) – were optimized from three starting configurations: one configuration in which the D-A geometries were "cofacial", and two configurations where the geometries were displaced longitudinally (one in each direction) by approximately one thiophene ring (see Scheme S7). In view of the large size of these systems, only the above three D-A complexes were studied for each combination.

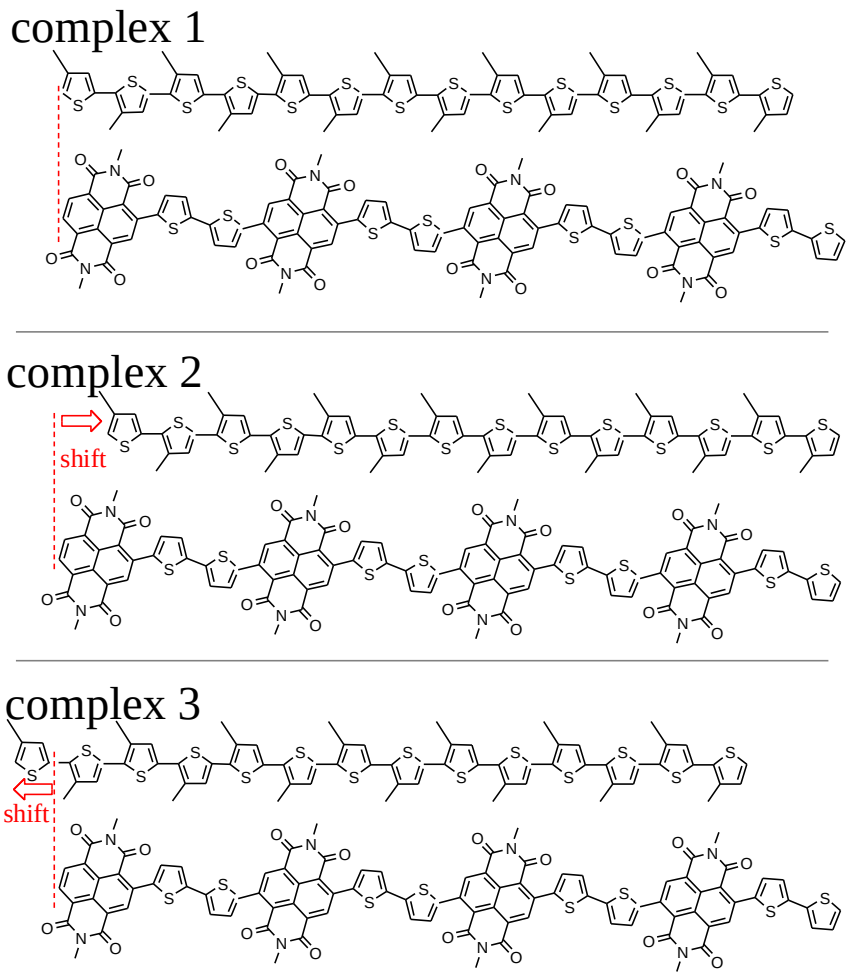

Scheme S7. Chemical structures of the donor- (upper structures) and acceptor (bottom structures) oligomers in the case of mP3HT-mNDI donor-acceptor combination. D-A Complexes 1 through 3 show schematically the three starting configurations before geometry optimization. D-A Complex 1 corresponds to the "cofacial" configuration, whereas D-A Complexes 2 and 3 represent two initial geometries where the 14-mer oligothiophene is longitudinally displaced by approximately one thiophene ring.

Density functional theory (DFT)[27] employing the B3LYP[28-29] functional in conjunction with the 6-31G* basis set was used for all calculations, except for the geometry optimization of D-D and A-A dimers and D-A complexes, in which the ωB97XD[30] functional was employed. This last choice is motivated by the necessity to consider long-range correction and include dispersion interactions during geometrical optimizations, both factors being absent in the case of B3LYP functional. Previous studies indicate that the calculations based on ωB97XD or other range-separated hybrid functionals with both default and optimally tuned range-separation (RS)

parameters (ω) strongly overestimate the energies of charge-transfer (CT) states.[31-32] In a very recent work[33] it was found that the estimated CT energies of small donor-acceptor complexes compare better with experiment when the RS parameter is optimized in the presence of a dielectric medium, in order to mimic the impact of the solid-state environment. Quite interesting, the tuning in the presence of a dielectric medium results in very small values of RS parameter, and CT energies that are comparable with that from B3LYP calculations. Indeed, our test calculations comparing the CT state energies for some of present systems with experimental values showed much smaller error when using B3LYP (0.1-0.2 eV) than in the case of ωB97XD (1 eV) functional.

Therefore, the evaluation of the excited-state properties of neutral D-D and A-A dimers and D-A complexes were obtained here by time-dependent (TDDFT)[34-38] calculations based on B3LYP functional. The B3LYP calculations were also used for the derivation of the intra-molecular reorganization energies.

CT rate constant calculations. The intramolecular reorganization energies (λ_i) were calculated according to the following equation (see also Scheme S8):[39]

$$\lambda_i = \lambda_i^1 + \lambda_i^2 = \left\{E_M^{GeometryM^+} - E_M^{GeometryM}\right\} + \left\{E_{M^+}^{GeometryM} - E_{M^+}^{GeometryM^+}\right\} \quad \text{(S1)}$$

In this equation, $E_M^{GeometryM}$ and $E_M^{GeometryM^+}$ correspond to the energy of the neutral molecule *M* in the neutral- and cationic geometries, whereas $E_{M^+}^{GeometryM}$ and $E_{M^+}^{GeometryM^+}$ correspond to the energy of the cationic species M^+ at the neutral- and cationic geometries.

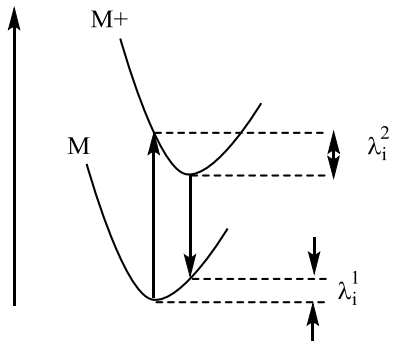

Scheme S8. Qualitative representation of potential surfaces of a neutral (M) and the corresponding cationic (M^+) species involved in the hole transfer. λ_i^1 and λ_i^2 correspond to two contributions to the intramolecular reorganization energy stemming from the geometrical deformations of the neutral- and cationic species, respectively.

The interoligomer electronic couplings (transfer integrals) were calculated within the fragment orbital approach.[40-42] The charge transfer rate was determined in the framework of the Marcus-Levich-Jortner equation:[43]

$$k_{CT} = \frac{4\pi^2}{h}\frac{1}{\sqrt{4\pi\lambda_s k_B T}} t^2 \sum_{n'=0}^{\infty} \exp(-S)\frac{S^{n'}}{n'!}\exp\left[\frac{-(\Delta G^\circ + \lambda_s + n'\hbar\omega_i)^2}{4k_B\lambda_s T}\right] \qquad \text{(S2)}$$

Here, t corresponds to the electronic coupling between molecular orbitals (MOs) located on two adjacent molecules, ΔG° is the reaction Gibbs free energy, λ_s is the reorganization energy of the medium, $S_i = \frac{\lambda_i}{\hbar\omega_i}$ is the Huang-Rhys factor, λ_i is the intramolecular reorganization energy.

The rate constants corresponding to charge separation were calculated separately for holes and electrons. While this model artificially splits the electron-hole separation in two seemingly "non-correlated" processes, it constitutes however a reasonable approximation at least in the limit case where the electron- and hole drift mobilities are very different.[16]

Energy Gradient (EG) calculations. The geometrical contributions to EG were calculated as simple differences between the orbital energies of the isolated fragments in two different geometries, extracted from the dimers and D-A complexes respectively (see Figure 8). The polarisation contributions[44] to the energy gradient were calculated according to the following equation:

$$\Delta(\mathrm{DCP}) = |\varepsilon_{H(L)}^{\text{isolated fragment}} - \varepsilon_{H(L)}^{\text{in the presence of the 2d fragment}}| \quad \text{(S3)}$$

In this equation, both HOMO(LUMO) energies are calculated at the same geometry, extracted either from D-D and A-A dimers or from D-A complexes. The notation "DCP" stands for "direct-contact polarization". The impact of the long-range polarization (LRP) contribution is missing in the EG values. However, it can be reasonably assumed that the LRP energy remains practically constant over few adjacent layers. Given that the energy gradient occurs over only few (roughly three) layers near the D-A interface,[13-14] a vanishingly small Δ(LRP) difference between two adjacent layers (our FSCS model) can be reasonably assumed, which justify the use of only the Δ(DCP) contributions in the EG values shown in Table 3.

It is worth noting that the present approach for calculating EG values additionally: (i) considers D-A complexes in neutral conditions, hence before exciton dissociation, (ii) ignores the dynamic polarization contributions in the real environment, and (iii) might overestimate the geometrical contribution. Consequently, the absolute EG values, despite the intriguingly good agreement with several experimental results,[13-15, 45] should be considered only as semi-quantitative ones. However, the global picture based in this frame is coherent and consistent with the experimental results, allowing producing reasonable qualitative trends, which is the goal of the present analysis.

All the calculations were carried out in vacuum by using the Gaussian09 suit of programs (Revision B.01).[46]

References

1. Schaftenaar, G.; Noordik, J. H., Molden: a pre- and post-processing program for molecular and electronic structures. *Journal of Computer-Aided Molecular Design* **2000,** *14* (2), 123-134.
2. Hush, N. S., Intervalence-Transfer Absorption. Part 2. Theoretical Considerations and Spectroscopic Data. *Progress in Inorganic Chemistry* **1967,** *8*, 391.
3. Hush, N. S., Homogeneous and heterogeneous optical and thermal electron transfer. *Electrochimica Acta* **1968,** *13* (5), 1005-1023.
4. Gould, I. R.; Noukakis, D.; Gomezjahn, L.; Young, R. H.; Goodman, J. L.; Farid, S., Radiative and Nonradiative Electron-Transfer in Contact Radical-Ion Pairs. *Chemical Physics* **1993,** *176* (2-3), 439-456.
5. Andersson, M. R.; Selse, D.; Berggren, M.; Jarvinen, H.; Hjertberg, T.; Inganas, O.; Wennerstrom, O.; Osterholm, J. E., Regioselective Polymerization of 3-(4-Octylphenyl)Thiophene With FeCl3. *Macromolecules* **1994,** *27* (22), 6503-6506.
6. Holcombe, T. W.; Norton, J. E.; Rivnay, J.; Woo, C. H.; Goris, L.; Piliego, C.; Griffini, G.; Sellinger, A.; Bredas, J.-L.; Salleo, A.; Frechet, J. M. J., Steric Control of the Donor/Acceptor Interface: Implications in Organic Photovoltaic Charge Generation. *Journal of the American Chemical Society* **2011,** *133* (31), 12106-12114.
7. Andersson, M. R.; Berggren, M.; Inganas, O.; Gustafsson, G.; Gustafssoncarlberg, J. C.; Selse, D.; Hjertberg, T.; Wennerstrom, O., Electroluminescence From Substituted Poly(Thiophenes) - From Blue to Near-Infrared. *Macromolecules* **1995,** *28* (22), 7525-7529.
8. Holcombe, T. W.; Woo, C. H.; Kavulak, D. F. J.; Thompson, B. C.; Frechet, J. M. J., All-Polymer Photovoltaic Devices of Poly(3-(4-n-octyl)-phenylthiophene) from Grignard Metathesis (GRIM) Polymerization. *Journal of the American Chemical Society* **2009,** *131* (40), 14160-1.
9. Chen, Z.; Zheng, Y.; Yan, H.; Facchetti, A., Naphthalenedicarboximide- vs Perylenedicarboximide-Based Copolymers. Synthesis and Semiconducting Properties in Bottom-Gate N-Channel Organic Transistors. *Journal of the American Chemical Society* **2009,** *131* (1), 8-9.
10. Marcus, R. A., On the Theory of Oxidation-Reduction Reactions Involving Electron Transfer. I. *J. Chem. Phys.* **1956,** *24*, 966.
11. Marcus, R. A., Electron transfer reactions in chemistry. Theory and experiment. *Rev. Mod. Phys.* **1993,** *65*, 599.
12. Marcus, R. A.; Sutin, N., Electron transfers in chemistry and biology. *Biochim. Biophys. Acta* **1985,** *811*, 265.
13. D'Avino, G.; Mothy, S.; Muccioli, L.; Zannoni, C.; Wang, L.; Cornil, J.; Beljonne, D.; Castet, F., Energetics of Electron-Hole Separation at P3HT/PCBM Heterojunctions. *Journal of Physical Chemistry C* **2013,** *117* (25), 12981-12990.
14. Ryno, S. M.; Risko, C.; Bredas, J.-L., Impact of Molecular Orientation and Packing Density on Electronic Polarization in the Bulk and at Surfaces of Organic Semiconductors. *ACS applied materials & interfaces* **2016,** *8* (22), 14053-62.
15. McMahon, D. P.; Cheung, D. L.; Troisi, A., Why Holes and Electrons Separate So Well in Polymer/Fullerene Photovoltaic Cells. *Journal of Physical Chemistry Letters* **2011,** *2* (21), 2737-2741.
16. Devizis, A.; De Jonghe-Risse, J.; Hany, R.; Nueesch, F.; Jenatsch, S.; Gulbinas, V.; Moser, J.-E., Dissociation of Charge Transfer States and Carrier Separation in Bilayer Organic Solar Cells: A Time-Resolved Electroabsorption Spectroscopy Study. *Journal of the American Chemical Society* **2015,** *137* (25), 8192-8198.

17. Schubert, M.; Collins, B. A.; Mangold, H.; Howard, I. A.; Schindler, W.; Vandewal, K.; Roland, S.; Behrends, J.; Kraffert, F.; Steyrleuthner, R.; Chen, Z.; Fostiropoulos, K.; Bittl, R.; Salleo, A.; Facchetti, A.; Laquai, F.; Ade, H. W.; Neher, D., Correlated Donor/Acceptor Crystal Orientation Controls Photocurrent Generation in All-Polymer Solar Cells. *Advanced Functional Materials* **2014,** *24* (26), 4068-4081.
18. Jo, J. W.; Jung, J. W.; Ahn, H.; Ko, M. J.; Jen, A. K.-Y.; Son, H. J., Effect of Molecular Orientation of Donor Polymers on Charge Generation and Photovoltaic Properties in Bulk Heterojunction All-Polymer Solar Cells. *Adv. Energy Mater.* **2016**, 1601365.
19. Kang, H.; Kim, K. H.; Choi, J.; Lee, C.; Kim, B. J., High-Performance All-Polymer Solar Cells Based on Face-On Stacked Polymer Blends with Low Interfacial Tension. *Acs Macro Letters* **2014,** *3* (10), 1009-1014.
20. Zhou, K.; Zhang, R.; Liu, J. G.; Li, M. G.; Yu, X. H.; Xing, R. B.; Han, Y. C., Donor/Acceptor Molecular Orientation-Dependent Photovoltaic Performance in All-Polymer Solar Cells. *Acs Applied Materials & Interfaces* **2015,** *7* (45), 25352-25361.
21. Ye, L.; Jiao, X. C.; Zhao, W. C.; Zhang, S. Q.; Yao, H. F.; Li, S. S.; Ade, H.; Hou, J. H., Manipulation of Domain Purity and Orientational Ordering in High Performance All-Polymer Solar Cells. *Chemistry of Materials* **2016,** *28* (17), 6178-6185.
22. Jung, J.; Lee, W.; Lee, C.; Ahn, H.; Kim, B. J., Controlling Molecular Orientation of Naphthalenediimide-Based Polymer Acceptors for High Performance All-Polymer Solar Cells. *Advanced Energy Materials* **2016,** *6* (15).
23. Richter, T. V.; Braun, C. H.; Link, S.; Scheuble, M.; Crossland, E. J. W.; Stelzl, F.; Wurfel, U.; Ludwigs, S., Regioregular Polythiophenes with Alkylthiophene Side Chains. *Macromolecules* **2012,** *45* (14), 5782-5788.
24. Kudla, C. J.; Dolfen, D.; Schottler, K. J.; Koenen, J. M.; Breusov, D.; Allard, S.; Scherf, U., Cyclopentadithiazole-Based Monomers and Alternating Copolymers. *Macromolecules* **2010,** *43* (18), 7864-7867.
25. Dolfen, D. Neue Donor-Akzeptor-Copolymere und Polyelektrolyte auf Perylenbasis. PhD, Bergische Universität Wuppertal, http://elpub.bib.uni-wuppertal.de/servlets/DocumentServlet?id=2920, 2012.
26. Kniepert, J.; Schubert, M.; Blakesley, J. C.; Neher, D., Photogeneration and Recombination in P3HT/PCBM Solar Cells Probed by Time-Delayed Collection Field Experiments. *Journal of Physical Chemistry Letters* **2011,** *2* (7), 700-705.
27. Kohn, W.; Sham, L. J., *Phys. Rev.* **1965,** *140*, A1133-A1138.
28. Becke, A. D., Density-functional thermochemistry. III. The role of exact exchange. *The Journal of Chemical Physics* **1993,** *98* (7), 5648-5652.
29. Lee, C. T.; Yang, W. T.; Parr, R. G., Development of the Colle-Salvetti Correlation-Energy Formula into a Functional of the Electron-Density. *Physical Review B* **1988,** *37* (2), 785-789.
30. Chai, J. D.; Head-Gordon, M., Long-range corrected hybrid density functionals with damped atom-atom dispersion corrections. *Phys. Chem. Chem. Phys.* **2008,** *10* (44), 6615-6620.
31. Yang, B.; Yi, Y. P.; Zhang, C. R.; Aziz, S. G.; Coropceanu, V.; Bredas, J. L., Impact of Electron De localization on the Nature of the Charge-Transfer States in Model Pentacene/C-60 Interfaces: A Density Functional Theory Study. *Journal of Physical Chemistry C* **2014,** *118* (48), 27648-27656.
32. Zhang, C. R.; Sears, J. S.; Yang, B.; Aziz, S. G.; Coropceanu, V.; Bredas, J. L., Theoretical Study of the Local and Charge-Transfer Excitations in Model Complexes of Pentacene-C-60 Using Tuned Range-Separated Hybrid Functionals. *Journal of Chemical Theory and Computation* **2014,** *10* (6), 2379-2388.

33. Zheng, Z. L.; Bredas, J. L.; Coropceanu, V., Description of the Charge Transfer States at the Pentacene/C-60 Interface: Combining Range-Separated Hybrid Functionals with the Polarizable Continuum Model. *Journal of Physical Chemistry Letters* **2016,** *7* (13), 2616-2621.
34. Casida, M. E.; Jamorski, C.; Casida, K. C.; Salahub, D. R., Molecular excitation energies to high-lying bound states from time-dependent density-functional response theory: Characterization and correction of the time-dependent local density approximation ionization threshold. *Journal of Chemical Physics* **1998,** *108* (11), 4439-4449.
35. Gross, E. K. U.; Kohn, W., Local density-functional theory of frequency-dependent linear response. *Phys. Rev. Lett.* **1985,** *55*, 2850-2852.
36. Gross, E. K. U.; Kohn, W., Time-dependent density-functional theory. *Adv. Quant. Chem.* **1990,** *21*, 255-291.
37. Runge, E.; Gross, E. K. U., Density-functional theory for time-dependent systems. *Phys. Rev. Lett.* **1984,** *52* (12), 997-1000.
38. Bauernschmitt, R.; Ahlrichs, R., Treatment of electronic excitations within the adiabatic approximation of time dependent density functional theory. *Chemical Physics Letters* **1996,** *256* (4-5), 454-464.
39. Bredas, J. L.; Beljonne, D.; Coropceanu, V.; Cornil, J., Charge-transfer and energy-transfer processes in pi-conjugated oligomers and polymers: A molecular picture. *Chemical Reviews* **2004,** *104* (11), 4971-5003.
40. Newton, M. D., Quantum Chemical Probes of Electron-Transfer Kinetics - The Nature of Donor-Acceptor Interactions. *Chemical Reviews* **1991,** *91* (5), 767-792.
41. Senthilkumar, K.; Grozema, F. C.; Bickelhaupt, F. M.; Siebbeles, L. D. A., Charge transport in columnar stacked triphenylenes: Effects of conformational fluctuations on charge transfer integrals and site energies. *Journal of Chemical Physics* **2003,** *119* (18), 9809-9817.
42. Valeev, E. F.; Coropceanu, V.; da Silva Filho, D. A.; Salman, S.; Bredas, J.-L., Effect of electronic polarization on charge-transport parameters in molecular organic semiconductors. *Journal of the American Chemical Society* **2006,** *128* (30), 9882-9886.
43. Jortner, J., Temperature dependent activation energy for electron transfer between biological molecules. *J. Chem. Phys.* **1976,** *64* (12), 4860-4867.
44. **We remember that, instead of energy contributions stemming from the interaction with- or between induced dipoles, the term "polarization" here includes (for historical reasons) principally contributions from electrostatic interactions.**
45. Sweetnam, S.; Graham, K. R.; Ndjawa, G. O. N.; Heumueller, T.; Bartelt, J. A.; Burke, T. M.; Li, W.; You, W.; Amassian, A.; McGehee, M. D., Characterization of the Polymer Energy Landscape in Polymer:Fullerene Bulk Heterojunctions with Pure and Mixed Phases. *Journal of the American Chemical Society* **2014,** *136* (40), 14078-14088.
46. Frisch, M. J.; Trucks, G. W.; Schlegel, H. B.; Scuseria, G. E.; Robb, M. A.; Cheeseman, J. R.; Scalmani, G.; Barone, V.; Mennucci, B.; Petersson, G. A.; Nakatsuji, H.; Caricato, M.; Li, X.; Hratchian, H. P.; Izmaylov, A. F.; Bloino, J.; Zheng, G.; Sonnenberg, J. L.; Hada, M.; Ehara, M.; Toyota, K.; Fukuda, R.; Hasegawa, J.; Ishida, M.; Nakajima, T.; Honda, Y.; Kitao, O.; Nakai, H.; Vreven, T.; Montgomery, J., J. A.; Peralta, J. E.; Ogliaro, F.; Bearpark, M.; Heyd, J. J.; Brothers, E.; Kudin, K. N.; Staroverov, V. N.; Keith, T.; Kobayashi, R.; Normand, J.; Raghavachari, K.; Rendell, A.; Burant, J. C.; Iyengar, S. S.; Tomasi, J.; Cossi, M.; Rega, N.; Millam, J. M.; Klene, M.; Knox, J. E.; Cross, J. B.; Bakken, V.; Adamo, C.; Jaramillo, J.; Gomperts, R.; Stratmann, R. E.; Yazyev, O.; Austin, A. J.; Cammi, R.; Pomelli, C.; Ochterski, J. W.; Martin, R. L.; Morokuma, K.; Zakrzewski, V. G.; Voth, G. A.; Salvador, P.; Dannenberg, J. J.; Dapprich, S.; Daniels, A. D.; Farkas, O.; Foresman, J. B.; Ortiz, J. V.; Cioslowski, J.; Fox, D. J., **2009,** *Gaussian 09, Revision B.01, Gaussian Inc., Wallingford CT, 2010.*